

© 2010

Aliye Özge Kaya

ALL RIGHTS RESERVED

CHANNEL MODELING APPROACHES TO WIRELESS SYSTEM DESIGN AND ANALYSIS

BY ALIYE ÖZGE KAYA

A dissertation submitted to the
Graduate School—New Brunswick
Rutgers, The State University of New Jersey
in partial fulfillment of the requirements
for the degree of
Doctor of Philosophy
Graduate Program in Electrical and Computer Engineering

Written under the direction of
Professor Wade Trappe and Professor Larry J. Greenstein
and approved by

New Brunswick, New Jersey

October, 2010

ABSTRACT OF THE DISSERTATION
Channel Modeling Approaches to Wireless
System Design and Analysis

by Aliye Özge Kaya

Dissertation Director: Professor Wade Trappe and
Professor Larry J. Greenstein

In wireless communications, it is common practice to use mathematical models for describing the radio channel. One approach is stochastic modeling, in which the key properties of the signal propagation (e.g., multipath fading) are captured by probability distributions. If the interest pertains to a specific environment, an alternative approach is to measure channel responses for a very large population of transmit-receive (T-R) paths; this is an effective but labor-intensive approach. An alternative approach that is less costly and more flexible is to use environment simulators. These are computer programs that (1) emulate the physical environment; (2) use wave propagation physics to predict the radio signal produced at any receive point from any transmit point; and (3) account for transmission through walls and diffraction around walls. This works best when the user has site-specific information on the geometry and structure materials. When the physical environment is well-specified, such as indoor areas where the layouts and materials of walls, floors and ceilings are known, environment simulation can be employed on a very large scale with very little effort.

In this thesis we focus on environment simulators based on ray-tracing. The major contribution is to demonstrate and evaluate the use of ray tracing for characterizing wireless channels and analyzing algorithms for various applications. We initially demonstrate, via comparisons with physical measurements, the statistical accuracy of ray-tracing predictions of channel behavior. The comparisons

are made for three parameters that largely characterize a radio path's behavior: Path loss; Ricean K-factor; and RMS delay spread. The comparisons show good agreement over the set of paths measured and simulated, establishing confidence that a well-designed radio simulator can be used reliably in system studies.

Environment-specific models generally assume the channel response is non-varying over time if both ends of the path are fixed. However, in real environments, channel responses vary over time, e.g. due to movement of objects (or people) near the transmission path. We have measured the channel response in an office building under different scenarios of environment dynamics. We stochastically modeled the time variation of the channel response about the mean using autoregressive processes and showed that this can lead to an accurate representation. Our approach could be used to model the time-varying tap gains to further augment the realism of ray-tracing simulations.

We then demonstrate several applications in wireless system design where ray-tracing could be exploited. First, we present an algorithm called Emitter Localization and Visualization (ELVIS) for localizing emitters by back-propagating the received signals via back-ray tracing. Second, we present a statistical path loss model derived from data simulated using a ray tracing tool. The characterization used is a nonlinear curve of the dB path loss to the log-distance, with a random variation about that curve due to shadow fading. Third, we devise an evaluation approach for densely populated urban wireless systems using MIMO links, wherein the location-specific channel gains are determined via ray-tracing. We compare and quantify the data rate performances of MIMO systems for various transmission schemes and antenna configurations; we present algorithms for adapting the MIMO transmission mode to varying channel conditions as a mobile moves along a given trajectory; and we treat the case of multiple bases to cover a full urban neighborhood and investigate the relationship among frequency reuse, co-channel interference and achievable data rate.

Acknowledgements

First and foremost, I would like to thank my advisors Prof. Wade Trappe and Prof. Larry J. Greenstein for their guidance, support, motivation and mentoring throughout my thesis. They made my PhD studies at Rutgers very enjoyable and rewarding.

Next, I would thank to Dr. Dmitry Chizhik from Bell Labs, Alcatel-Lucent for collaborating with me throughout my thesis on various topics and for being on my committee. Many thanks to Prof. Narayan Mandayam for being in my committee. I would also thank Dr. Reinaldo Valenzuela from Bell Labs, Alcatel-Lucent and Prof. Mung Chiang from Princeton University for collaborating with me on various topics.

My special thanks goes to the many friends I made at WINLAB. We spent many memorable times together.

Last but not least, I would thank to my parents Zehra Nur and Oktay for their support and encouragement throughout my studies.

Dedication

To my parents Zehra Nur and Oktay

Table of Contents

Abstract	ii
Acknowledgements	v
Dedication	vi
List of Tables	xii
List of Figures	xiii
1. Introduction	1
2. Characterizing Indoor Wireless Channels via Ray Tracing and Validation via Measurements	5
2.1. Introduction	5
2.2. Methodology	7
2.2.1. Measurements with a Vector Network Analyzer (VNA)	7
2.2.2. Simulations with the WiSE Tool	7
2.3. K-factor Estimation Methods	8
2.3.1. Prior Work on Ricean K-factor Estimation	8
2.3.2. Estimation from Impulse Responses	9
2.3.3. Estimation from Frequency Responses: Coherent Method	9
2.3.4. Estimation from Frequency Responses: Moment Method	10
2.4. RMS Delay Spread	10

2.5.	Comparing VNA Data and WiSE Predictions	11
2.5.1.	Transmitter-Receiver Paths Measured	11
2.5.2.	Wall Properties	12
2.5.3.	Path Gain, K-factor and Fade CDFs	13
2.5.4.	RMS Delay Spread	14
2.6.	Conclusion	15
3.	Modeling Temporal Channel Variations in Indoor Wireless En-	
vvironments	17
3.1.	Introduction	17
3.2.	Measured Environments	19
3.3.	Time Variation in Measured Environments	20
3.3.1.	Static Environment	20
3.3.2.	Quasi Static Environment	21
3.3.3.	Random Movement	21
3.3.4.	Office Space	22
3.4.	Time Variation Modeling	22
3.4.1.	Prior Work on Autoregressive Processes	22
3.4.2.	Autoregressive Integrated Moving Average (ARIMA) Mod-	
	els of the Variations	23
3.5.	ARIMA Modeling and Results	23
3.5.1.	Quasi-Static Case	24
	Identification	24
	Mean and Variance	24
	Auto Correlation Function (ACF)	25
	Partial Correlation Function (PCF)	25
	Choosing the possible models	26

Estimating Parameters	26
Diagnostic Check	26
3.5.2. Random-Movement Case	28
3.5.3. Office Space	28
3.6. Conclusion	29
 4. Emitter Localization and Visualization (ELVIS):	
A Backward Ray Tracing Algorithm for Locating Emitters	30
4.1. Introduction	30
4.1.1. Prior Work	30
4.1.2. Our Contributions	30
4.2. WISE (Wireless System Engineering)	32
4.3. Backward Ray Tracing in ELVIS	32
4.4. Emulating Degradations	33
4.5. ELVIS	33
4.5.1. Basic Algorithm	33
4.5.2. Multiple Receivers	34
4.6. Simulation results	35
4.6.1. Perfect Measurements	35
Single Receiver	35
Multiple Receivers	36
4.6.2. Degraded Measurements	36
Single Receiver	36
Multiple Receivers	37
4.7. Conclusion	37
 5. An Empirically Based Path Loss Model for Wireless Channels in	
Indoor Environments	39

5.1.	Introduction	39
5.2.	Data Collection	39
5.2.1.	WISE Simulations for AT&T Building in Middletown, NJ	40
5.2.2.	WISE Simulations for the Hynes Convention Center in Boston, MA	40
5.2.3.	WISE Simulations for the Alcatel-Lucent Building in Holmdel, NJ	41
5.2.4.	WISE Simulations for a Curved Office Building	42
5.3.	Path Loss Model and Results	42
5.4.	Conclusions	45
6.	Calculating MIMO Performance in Urban Microcells Using Ray- Tracing	48
6.1.	Introduction	48
6.2.	Location-Specific MIMO Performance in Urban Wireless Channels	50
6.2.1.	Motivation	50
6.2.2.	Simulation Method	51
6.2.3.	Results	52
	Array Size and Transmit Power	53
	Polarization	53
	Diffraction	54
	Array Orientation	55
	Antenna Height	56
	Approach Based on Rayleigh Fading	57
	Different Cities and Neighborhoods	58
	Transmission Scheme	59
6.3.	Adapting MIMO Transmission Mode Along Paths in Urban Envi- ronments	60

6.3.1. Motivation	60
6.3.2. Related Work	61
6.3.3. Optimal Switching (OS)	61
6.3.4. Delayed Feedback (DF)	61
6.3.5. Probabilistic switching (PS)	62
6.3.6. Performance Metrics	63
6.3.7. Results	63
6.4. MIMO Base Station Deployment in Urban Cells	64
6.4.1. Motivation	64
6.4.2. Base Deployment for a Minimum-SNR Requirement	65
6.4.3. Frequency Reuse	66
6.4.4. Results	67
6.5. Conclusions	70
7. Conclusions and Future Work	72
Appendix A.	77
A.1. Models for Time Series Data	77
A.1.1. The Autoregressive (All-Poles) Processes, AR	77
A.1.2. The Moving Average (All-Zeroes) Processes, MA	77
A.1.3. The Autoregressive Moving Average Processes, ARMA	78
A.1.4. ARIMA	78
References	80
Curriculum Vitae	85

List of Tables

2.1. Comparision WiSE and VNA data	15
5.1. Parameters of the Path Loss Model	45
6.1. Average Downlink Achievable Rate, in Gb/s per km ²	70

List of Figures

2.1. Transmitter-receiver locations within ORBIT lab: $T \rightarrow R$, $A \rightarrow B$ and $T1 \rightarrow C$ to $T16 \rightarrow C$	12
2.2. Comparison of CDF's of path gain ($T \rightarrow R$). The curves shown with K-factor are the Ricean CDFs. The VNA-derived, and WISE- predicted CDFs look like one another and like the Ricean CDFs. .	14
3.1. Ratio of the trial power gain P_{trial} to the average power gain P_{avr} versus trials (Quasi-Static Environment)	21
3.2. Ratio of the tap power gain to average power gain versus tap num- ber (Quasi-Static Environment)	22
3.3. Mean and standard deviation (Quasi-Static Environment)	24
3.4. Auto Correlation Function (Quasi-Static Environment)	25
3.5. Partial Correlation Function (Quasi-Static Environment)	26
3.6. AR(3) process compared with data (Quasi-Static Environment) .	27
3.7. Comparison of autocorrelation function of the data and AR(3) pro- cess (Quasi-Static Environment)	27
3.8. AR(14) process compared with data (Random Movement)	28
3.9. ARIMA(15,1,0) model compared with data (Office Space)	29
4.1. Backward ray tracing: Each ray becomes a new arrival at the ef- fective point of incidence	32
4.2. WISE output: Radio paths between receiver and emitter in the Crawford Hill building. This building is about 120 m x15 m . . .	35

4.3. CDF of Prediction Error by perfect measurement of power, TOA and AOA	36
4.4. CDF of Prediction Error using 20 degree angular bins and various degradations	37
5.1. Building plan of AT&T Middletown Building	40
5.2. Building plan of Hynes Convention Center in Boston	41
5.3. Building plan of Crawford Hill Building	41
5.4. Curved office Building	42
5.5. Path Loss versus distance	43
5.6. Sample means of the path loss values in each distance bin	44
5.7. Curve fits to the mean curves in Fig. 5.6	46
5.8. Standard deviations about the mean path loss curves	46
5.9. CDF of the shadow fading component for the curved office building. A straight line denotes Gaussian distribution. This case is typical for the other buildings we considered.	47
5.10. Comparison of standard deviations from the linear fit using the conventional path loss model with the stand deviations from the exponential fit in (5.3) for the Crawford Hill Building	47
6.1. Street plan in Manhattan. Three paths are shown: 1) The trans- mitter is fixed at A and the receiver moves from P1 to P2, a 274-m LOS path on Park Avenue. 2)The transmitter is fixed at B and the receiver moves from P3 to P4, a 323-m LOS-path on Lexington Avenue. 3) The transmitter is fixed at B and the receiver moves from P5 to P6, a 50-m NLOS-path on East 103 rd Street.	52

6.2.	CDFs of capacity for 4x4 MIMO for various polarization types along the Park Avenue path in Fig. 6.1. Use of vertically polarized dipoles yield more capacity than the horizontally-polarized dipoles. Including diffraction effects does not change the CDF perceptibly.	54
6.3.	CDFs of capacity for 4x4 MIMO with vertically polarized dipole antennas, both with and without diffraction effects considered for the LOS path P1-P2 along Lexington Avenue, for the NLOS path P3-P4 on the East 103 rd Street in Fig. 6.1 and for a 20-m NLOS path in Boston. The CDFs are only slightly different on the paths P1-P2 and P3-P4. On a NLOS path in Boston diffraction has more effect on the paths in Fig. 6.1.	55
6.4.	CDFs of capacity, for horizontally and vertically oriented arrays, for the Park Avenue path in Fig. 6.1. Use of horizontally oriented arrays yields an average capacity increase of 11 bps/Hz, corresponding to a 68 % improvement over using vertical arrays.	56
6.5.	The highest average capacity is obtained when the transmitter and receiver antennas are at the same height.	57
6.6.	CDF of capacity for 4x4 MIMO on the LOS-path along Lexington Ave and along the NLOS path along 103 rd street in Fig. 6.1. The dashed curve is obtained from H-matrices predicted via ray tracing; the solid curve corresponds to assuming Rayleigh channel gain matrices. The Rayleigh assumption is wildly optimistic and unreliable way for estimating performance on LOS paths. On the NLOS path, the CDFs have much better agreement than on the LOS path.	58
6.7.	CDF of capacity for five different paths at varying neighborhoods both in Boston and Manhattan	59

6.8. Achievable rate on the Lexington Avenue path, P3-P4, in Fig. 6.1 versus the distance from P3. Each data rate is averaged over a 1-m window. SM is seen to be the best transmission mode to use at most locations.	60
6.9. M=856 receiver locations and L=177 candidate base locations. We want to choose the minimum number of base stations such that the SNR at each receiver location is above an SNR-threshold (chosen here to be 20 dB).	68
6.10. CDFs of achievable rate for system with 4x4 MIMO links for r=1, 2, 3, 4 (Small Area)	69
6.11. CDFs of achievable rate for various array sizes and r=1 (Large Area).	70

Chapter 1

Introduction

Motivation

In wireless communications, the underlying radio channel properties strongly affect the performance of the system. It is common practice in the design and evaluation studies of such systems to use mathematical models for describing the channel. One approach is stochastic modeling, in which the key properties of the signal propagation (e.g., multipath fading) are captured by probability distributions. These kinds of models are favored when the propagation environment is unknown except for some high-level attributes, e.g., urban vs. suburban, flat vs. hilly, summer vs. winter, etc.

Stochastic models serve well when the study questions are fairly generic, e.g., how does a particular cellular radio system perform in an environment that is typically urban? However, there are cases where the interest pertains to a specific environment, e.g., a wireless LAN in the corporate offices of a specific company, a mobile moving along a given trajectory, coverage of users in a given specific urban neighborhood. In such cases, the study questions are ‘site-specific’ and so site-specific channel response information is needed. One very effective approach in that case might be to measure channel responses for a very large population of transmit-receive (T-R) paths and store them in a database that can be accessed for system simulations. The number of such paths that must be sampled, however, can be extremely large and require measurement campaigns that are long, labor-intensive and costly.

A far less costly alternative to measurements is to use *environment simulators*. These are computer programs that (1) emulate the physical environment; (2) use wave propagation physics to predict the radio signal produced at any receive point from any transmit point; and (3) account for transmission through walls and diffraction around walls. This works best when the user has site-specific information on the geometry and structure materials of the area being studied. When the physical layout is well-specified, such as indoor areas where the layouts and materials of walls, floors and ceilings are known, environment simulation can be employed on a very large scale with very little effort.

Related Work

Ray-tracing based methods are popular for predicting the site-specific radio propagation characteristics [1], [2], [3], [4]. Although they are computationally intensive they provide more accurate results than statistical models [1] when the site geometries are known.

For urban microcell environments [5] and [6] show very good agreement between the signal strength (or path loss) statistics of environment simulators based on ray-tracing and those from extensive measurements. In [6] the comparisons are done for data collected in a two-square kilometer area of Rosslyn, Washington DC, and in [5] the comparisons are done for data collected in Manhattan and Boston. The comparisons show that ray-tracing based simulators can predict signal strengths in these outdoor environments with very good accuracy.

For indoor channels, [2] shows that the distributions of arrival times and angular spreads generated with a ray-tracing tool agree excellently with those of an empirical model based on measurements. In [7], extensive measurements in several office buildings are used to derive statistics for the K factor and path loss, which favorably compare with ray-tracing predictions.

All of these results demonstrate the validity of using a ray tracing tool for modeling indoor and outdoor channels.

Summary of the Thesis

In this thesis, we focus on environment simulators based on ray-tracing. The major contribution is to demonstrate and evaluate the use of ray tracing for characterizing wireless channels and analyzing algorithms for various applications. We initially demonstrate, via comparisons with physical measurements, the accuracy of ray-tracing in predicting static channel behavior. We also augment the realism of such ray-tracing simulations by modeling the time-varying part of the channel response, as caused by moving objects in the environment, using stochastic processes. We then demonstrate several applications in wireless system design where ray-tracing can be exploited.

The thesis is organized as follows:

In Chapter 2, we investigate the reliability of radio channel simulators based on ray tracing in predicting channel response behavior throughout a well-specified environment. We assess the performance of this approach by comparing its predictions with measurements in a specific static environment. The good agreement on path loss statistics, Ricean K-factor and RMS delay spread, over the set of paths measured and simulated, suggests that a well-designed radio simulator can be used reliably to predict system behavior.

In Chapter 3, we propose ways to augment ray-tracing simulations by treating the time-varying part of the channel response using stochastic processes. Environment-specific models generally assume the channel response is non-varying over time if both ends of the path are fixed. However, in real environments channel response varies over time, e.g. due to movement of objects (or people) in the environment. We have measured the channel response in an office building

under different environmental dynamics scenarios. We stochastically model the time variation of the response about the mean using autoregressive processes and show that this leads to good representations.

In Chapter 4, we propose an algorithm called Emitter Localization and Visualization (ELVIS) for localizing emitters based on backward ray tracing. Our work uses the backward ray tracing for the first time for indoor emitter location prediction. In an emergency situation like fire it is important to localize the personnel such that police, fire-fighters etc. We assume that the first responder emits RF energy, which undergoes multiple reflections with the walls, ceilings and floors of the building. There are K receivers, each of which receives ray(s) from the first responder. Each receiver estimates the AOA (Angle of Arrival), TOA (Time of Arrival) and power of each ray. We assume that the receivers know the blueprint of the building and the electromagnetic characteristics of the construction material used in the building. We show that, based on this information, the receivers can localize the first responder to a high degree of accuracy by applying ELVIS. We evaluated the performance of ELVIS, using both single and multiple receivers, under a variety of channel and propagation conditions.

In Chapter 6, we use the ray tracing tool for modeling path loss in indoor environments. The proposed path loss model takes into account the transmission losses through the walls and leads to a median path loss that is nonlinear in log-distance, in contrast to conventional models. One application could be the use of environment simulators for a specified building for each of N base locations, with N on the order of 8-12, to find a set of path loss model parameters. Using the path loss model system planners can determine where to put bases to best cover the area for a given system, and they do not have to store millions of data points, just a relatively small number of parameters.

Chapter 2

Characterizing Indoor Wireless Channels via Ray Tracing and Validation via Measurements

2.1 Introduction

It is axiomatic that no typical environment can be perfectly emulated. Propagating radio signals are affected by countless artifacts that are hard to capture and/or predict, i.e., moldings, variations in material, furniture, etc. What can reasonably be expected, however, is that a site-specific program predicts channel responses throughout the area of interest that are statistically similar to the actual ones. To this end, we can cite three parameters of a radio path that largely typify its response for both narrow and wide bandwidths. They are: (1) the *path loss*, PL , which is the dB value of the transmit power divided by the (locally averaged) received power; (2) the *Ricean K -factor*, which, together with PL , dictates the narrowband fading distribution; and (3) the *RMS delay spread*, τ_{rms} , which is a measure of the frequency selectivity (or pulse dispersion) of the channel. We assert that a site-specific program that accurately predicts these three quantities throughout a known environment can be relied upon to predict performance in that environment.

In this chapter, we consider a particular environment, namely, the ORBIT Laboratory of Rutgers University's WINLAB [8, 9]; and we test a particular simulator, namely, the Wireless Systems Engineering (WiSE) Tool, a ray-tracing program developed by Bell Labs [4]. For a total of 18 chosen transmit-receive (T-R) paths, we use a Vector Network Analyzer (VNA) to measure complex

frequency responses over a wide bandwidth, i.e., from 3 to 4 GHz; and we use WiSE to predict the impulse response. From both, we can compute (and make comparisons for) the path loss, K-factor and RMS delay spread. Our findings underscore the importance of accurately specifying the electrical properties of the surfaces (walls, etc.) in addition to their layouts.

There is related published work in this area. For urban microcell environments [10] shows very good agreement between the signal strength (or path loss) statistics of WiSE and those from extensive measurements. For indoor channels, [2] shows that the distributions of arrival times and angular spreads generated with WiSE agree excellently with those of an empirical model based on measurements. In [7], extensive measurements in several office buildings are used to derive statistics for K factor and path loss, which favorably compare with WiSE predictions. All these results demonstrate the validity of using a ray tracing tool. In this paper, we add to prior results on K-factor and path loss; add new results for RMS delay spread; and show that a certain amount of preliminary trial-and-error (measurement, comparison and adjustment) can enhance the accuracy of such a tool.

The chapter is organized as follows. In Section 2.2, we describe the measurement and ray-tracing simulation methods used here. Sections 2.3 and 2.4 describe, respectively, K-factor estimations derived from channel response data and the estimation of RMS delay spread. Section 2.5 compares WiSE predictions with VNA measurements in terms of path gain, K-factor and RMS delay spread.

2.2 Methodology

2.2.1 Measurements with a Vector Network Analyzer (VNA)

In our experiments, we measured the complex channel response with the Agilent E5071B vector network analyzer (VNA) . Measurements were carried out at various locations in the ORBIT room and office area of WINLAB, Rutgers University. The ORBIT room is of size 20 m×25 m and it is surrounded by offices, cubicles and hallways. The office area of WINLAB is as big as the ORBIT laboratory but contains cubicles, lots of furniture and small office rooms.

All antennae were omnidirectional, at the same height, 1.25 m, and all transmit powers were 10 dBm. The VNA measured the complex frequency response at N equally spaced frequencies over a given frequency range. We did M trials at each specific location. The time duration between the contiguous trials was two seconds. This corresponds to the time spent for measuring the frequency response at N points, and then processing and transferring the data over the network. The impulse response in each trial was found via the inverse Fourier transform of the complex frequency response. The resulting time sequence, $h(n)$ represents the complex envelope of the response, sampled at 1 ns intervals and referred to 3.5 GHz. Each term in the sequence can be regarded as a ray.

2.2.2 Simulations with the WiSE Tool

We used WiSE [4] to simulate the static radio environment of the ORBIT room where we conducted the VNA measurements. Given a building plan and transmitter location, WiSE simulates the impulse response for any path in the building as a sum of rays. It accounts for the many rays that undergo reflection and transmission, where the number of reflections included per ray is a program input. It

takes into account path loss and the wall layer properties, such as dielectric coefficient, width, conductivity, number of layers, etc. In WiSE, each wall is defined by its geometric layout and by a parameter called ‘wall type’. An existing wall type can be redefined or a new wall type can be defined by declaring dielectric coefficients, width and conductivity for each layer of the wall.

2.3 K-factor Estimation Methods

2.3.1 Prior Work on Ricean K-factor Estimation

The K-factor is the ratio of the power in the line-of-sight (LOS) component to the total power of the non-LOS (NLOS) components. It is a measure of the extent of fading on the link, where lower K means deeper fading while a higher K-factor would correspond to a more Ricean environment.

Various algorithms have been proposed to estimate the K-factor. The moment method reported in [11] estimates the K-factor from the second and fourth moments of the signal fading variation over time, space or frequency. It is more practical than many other proposed methods, as it requires power samples only (no phase). The moment method can be generalized to use with different moments, as in [12]. The authors in [12] also propose a K-factor estimation method using the in-phase and quadrature components, but this method is applicable only to narrow band signals. The method of maximum likelihood (ML) estimation of K-factor is proposed in [13], wherein the parameters of the Ricean distribution are chosen as those parameters which maximize the joint probability density of the observed outcomes.

2.3.2 Estimation from Impulse Responses

The channel impulse response gives the rays received at different delays. The ray that has the largest magnitude is designated as the line-of-sight “LOS” component. The power sum of the other remaining rays constitute the “scatter” power. The ratio of the LOS ray’s power to the scatter power gives the K-factor.

Note that the physical LOS component is almost always the one with the shortest delay. Thus, the power we use for the K-factor numerator may or may not be the actual LOS power. From the standpoint of estimating a K-factor that accurately predicts the fading distribution, however, this is an intuitive approach that (as we will show) leads to excellent results.

2.3.3 Estimation from Frequency Responses: Coherent Method

The K-factor can be computed from the complex frequency response coherently. Assume we know the complex channel response $H(f)$ at M different frequencies. Let $V = |V|e^{-j\phi}$ be the complex amplitude of the LOS component. It can be estimated by minimizing the difference between the expected and measured channel response. Thus,

$$V^* = \arg \min_V E_f\{|H(f) - |V|e^{-j(2\pi f\tau + \phi)}|^2\} \quad (2.1)$$

where τ is the delay at which the LOS component is received. The solution V^* to this minimization problem is

$$V^* = E_f\{H(f)e^{j2\pi f\tau}\}, \quad (2.2)$$

where τ is found as

$$\tau^* = \arg \max_{\tau} E_f\{|H(f)e^{j2\pi f\tau}|\}. \quad (2.3)$$

This solution is equivalent to performing an inverse Fourier transform on the frequency domain data and choosing the largest component as the LOS component.

Therefore, the coherent method gives the same result as estimating the numerator of the K-factor from the most powerful ray of the impulse response.

2.3.4 Estimation from Frequency Responses:

Moment Method

The moment method proposed in [11] assumed a temporal variation of the received signal. It uses the second and fourth moments of the magnitude variation over some long interval for the K-factor estimation. This method needs only the absolute values of the received signal samples. It is also applicable to frequency domain data, assuming a very wide bandwidth. Thus, the K-factor can be computed by computing second and fourth moments from the samples of $|H(f)|$.

This method loses precision at very low K-factors, i.e., $K \leq 1$. At the same time, the fading distribution does not change much over that range of K , so that imprecision in estimating K is not impactful.

2.4 RMS Delay Spread

The RMS delay spread is a measure of the frequency selectivity (or pulse dispersion) of a link. Pulse dispersion arises as a result of the signals taking different times to cross the channel through different propagation paths. The RMS delay spread is defined as the second central moment of the power delay profile:

$$\tau_{rms} = \sqrt{\bar{\tau}^2 - \bar{\tau}^2}, \quad (2.4)$$

where

$$\bar{\tau} = \frac{\sum_{n=1}^N P_n t_n}{\sum_{n=1}^N P_n}; \quad \bar{\tau}^2 = \frac{\sum_{n=1}^N P_n t_n^2}{\sum_{n=1}^N P_n}, \quad (2.5)$$

N is the number of received rays; and P_n and t_n are, respectively, the power and arrival time of n^{th} ray ¹.

$$\tau_{rms} = \frac{1}{\sum_{n=1}^N P_n} \sqrt{\sum_{n=1}^N \sum_{m=n+1}^N P_n P_m (t_n - t_m)^2}. \quad (2.6)$$

We can rewrite (2.6) as

$$\tau_{rms} = \sqrt{\sum_{n=1}^N \sum_{m=n+1}^N \rho_n \rho_m (t_n - t_m)^2} \quad (2.7)$$

where ρ_x is the normalized power of x^{th} ray,

$$\rho_x = \frac{P_x}{\sum_{n=1}^N P_n}. \quad (2.8)$$

Clearly, $0 \leq \rho_x \leq 1$. From (2.7) it is obvious that RMS delay spread depends only on delay differences, and does not depend on where we set the origin, $\tau = 0$. It also does not depend on the transmit power, but solely on the power ratios of the rays.

2.5 Comparing VNA Data and WiSE Predictions

2.5.1 Transmitter-Receiver Paths Measured

We report here on VNA-WiSE comparisons for 18 different transmitter-receiver paths in the ORBIT lab. We repeated such experiments for various other paths and found similar results. Specifically, we measured the complex frequency response at 1601 points between 3.0 and 4.0 GHz. We repeated this VNA experiment 50 times for each path. Since the differences among the experiments were small, we show the results for only instance among 50. We chose the frequency range as 3-4 GHz to avoid interference from the widely used 2.4 and 5

¹We can regard P_n as the squared magnitude of the n^{th} ray in the impulse response, as described in Section 2.2.1 for the VNA data and in Section 5.2 for WiSE. Also, N is not necessarily the same for the VNA-derived and WiSE-derived impulse responses.

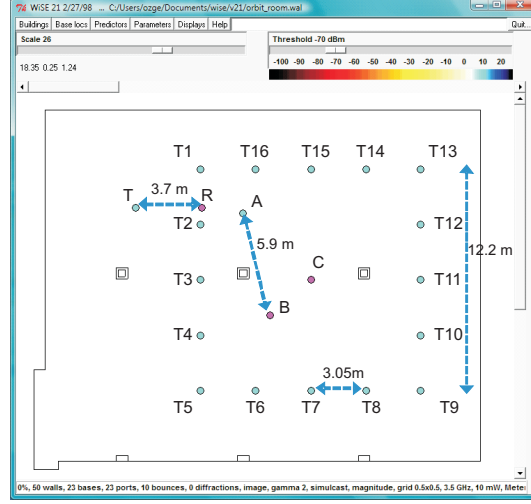


Figure 2.1: Transmitter-receiver locations within ORBIT lab: $T \rightarrow R$, $A \rightarrow B$ and $T1 \rightarrow C$ to $T16 \rightarrow C$

GHz bands. Fig. 2.1 shows the 18 transmitter-receiver paths $T \rightarrow R$, $A \rightarrow B$ and from $T1 \rightarrow C$ to $T16 \rightarrow C$. T and R are 3.6 m apart; and A and B are 5.9 m apart. The transmitter locations $T1$ to $T16$ are located on a square of size 12.2 m x 12.2 m, where neighboring transmitter locations are about 3 m apart. The receiver location C is at the center of this square.

2.5.2 Wall Properties

The walls in the ORBIT lab are made of multiple layers of different materials used for isolation and shielding. Moreover, not every wall has the same layers; and we do not have exact information on the properties of these layers. Therefore, modeling of the walls is not straightforward. We considered, for each wall, various predefined wall types in WiSE. We have chosen those wall types for which preliminary experiments and comparisons between VNA and WiSE results showed the best agreement. For the ceiling and floor we chose a concrete wall type, for the other walls, we chose metallic and sheetrock wall types.

The pillars on the radio path cause diffraction, reflection and transmission,

which affect the received power significantly. Therefore, accurate modeling of the pillars is necessary. We modeled the pillar walls using a sheetrock wall type. We know that each pillar is built with a metallic block inside. Therefore, we added a second layer of walls made of metal inside the pillars. During our search for the best wall type combinations, we learned how critical the electrical properties of the walls are in addition to their geometric layout. We conclude that a certain amount of preliminary trial-and-error (measurement, comparison and adjustment) is needed for the prediction tool to be confidently applied.

2.5.3 Path Gain, K-factor and Fade CDFs

The cumulative distribution function (CDF) of the path gain (power ratio) can be obtained directly by sorting the measured or simulated frequency response samples. We call this the empirical CDF. A good fit to this curve is found in every case to be the theoretical Ricean CDF, parameterized only by the K-factor and average power gain.

Fig. 2.2 compares the path gain CDF's for the path $T \rightarrow R$. We see that the theoretical curves (obtained for K-factors estimated using either the moment method or the impulse response method) are very good matches to the empirical CDF's. Also, the WiSE-based and VNA-based CDF's of path gain are very close to each other. We obtained similarly good matches also for the other 17 links. Table 6.1 summarizes the average path gains and the variation of the K-factors for the 18 paths considered. The measured and predicted values are seen to be in good agreement. Additionally, our results show that, in indoor environments, the K-factor is very low due to the transmissions through and reflections from the walls and objects in the surrounding. The maximum K-factor we saw was 1.42.

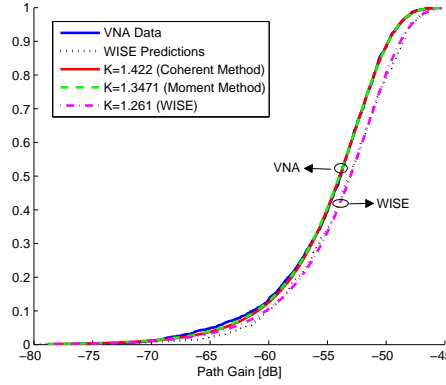


Figure 2.2: Comparison of CDF's of path gain ($T \rightarrow R$). The curves shown with K-factor are the Ricean CDFs. The VNA-derived, and WISE-predicted CDFs look like one another and like the Ricean CDFs.

2.5.4 RMS Delay Spread

The RMS delay spread, τ_{rms} , depends solely on the delay differences among the rays and on their relative powers, (7). Because the delay spread is based on moments of a function, impulse response rays at the larger delays can have an important impact on the calculated result, even if their powers are very low. The VNA-derived impulse response, being an inverse Fourier transform of measured frequency response samples, has rays out to a maximum delay dictated by the measurement bandwidth (1 GHz) and the number of samples (1601), i.e., out to $1.6 \mu s$. This is much larger than the actual maximum delay in an indoor environment. The additional 'rays' in the VNA-derived impulse response are the result of measurement noise and other measurement artifacts.

To fairly compare the VNA-derived τ_{rms} with the value predicted using WiSE, we should use a maximum delay, t_η , that is common to both calculations. We chose the delay at which the WiSE ray powers drops permanently below -30 dB relative to the strongest ray in the impulse response. Thus, from both the VNA-derived and WiSE-predicted impulse responses, we calculate RMS delay spread using rays from relative delay 0 to relative delay t_η .

Table 2.1: Comparison WiSE and VNA data

	Av. Path Gain [dB]		K		RMS d. s. [ns]	
	VNA	WiSE	VNA	WiSE	VNA	WiSE
T→R	-53.01	-52.04	1.42	1.26	41	34
A→B	-56.29	-55.18	0.58	0.82	58	48
T1→C	-56.07	-57.05	0.19	0.46	67	52
T2→C	-54.38	-56.52	0.20	0.82	62	51
T3→C	-56.86	-55.27	0.16	0.73	73	56
T4→C	-54.21	-55.97	0.28	0.66	60	53
T5→C	-55.55	-56.40	0.22	0.38	68	57
T6→C	-53.63	-55.44	0.24	0.54	61	61
T7→C	-53.18	-55.08	1.13	0.68	58	56
T8→C	-53.60	-55.76	0.30	0.61	60	56
T9→C	-54.21	-56.15	0.31	0.35	61	55
T10→C	-53.42	-55.51	0.53	0.56	65	58
T11→C	-56.96	-56.13	0.36	0.32	74	56
T12→C	-55.04	-55.99	0.30	0.67	71	57
T13→C	-57.74	-55.83	0.10	0.52	68	58
T14→C	-55.99	-55.69	0.13	0.59	66	52
T15→C	-55.13	-55.14	0.29	0.69	64	55
T16→C	-55.63	-55.23	0.08	0.50	64	54

The RMS delay spreads for 18 links are shown in Table 1. They differ in most cases by 20 percent or less, with the VNA-derived estimates always being higher. In just a few cases, the VNA-derived value is as much as 30 percent higher.

The consistent increase of VNA-derived values over WiSE predictions may be due to imperfect calibration of the VNA data. The VNA-derived delay spread can be shown to be sensitive to calibration errors, and in a way that would increase its estimated value (c.f., [14]). Correcting for this impairment would improve the comparisons shown. This bears further study.

2.6 Conclusion

The comparisons in Table I for the 18 paths we studied show that the parameters predicted using WiSE agree well with measurements. This suggests that a well-designed ray-tracing program such as WiSE can be used with confidence for

studying systems in indoor wireless environments.

In the course of our investigation, we identified two conditions that can compromise prediction accuracy of critical path properties: (1) Paths where diffraction is the primary propagation mechanism; and (2) environments for which the material properties of the walls, floor and ceiling are not well-specified. The first condition is relatively rare in indoor environments; the second condition can be avoided by using a small number of preliminary measurements, augmented by comparisons with predictions and corresponding adjustments of the assumed material properties.

Further work in this area should include, primarily, its extension to other paths and to other indoor environments. In addition, a limited amount of system studies would help to test the conjecture that the parameters studied here (path gain, K-factor and RMS delay spread) comprise a sufficient set for capturing the properties of a channel response.

Chapter 3

Modeling Temporal Channel Variations in Indoor Wireless Environments

3.1 Introduction

Published models, whether stochastic or environment-specific, generally assume the channel response is non-varying over time if both ends of the path are fixed. However, in real environments channel responses vary over time, e.g. due to movement of people in the environment. A question that has been open in the propagation community is whether this variation is negligible, and how it can be modeled in cases where the variation is not negligible. Here, we examine this problem. We have measured the channel response in an office building under different scenarios of environmental dynamics (i.e., movement of people), and we have identified stochastic processes to characterize them.

If there is considerable motion of people in an otherwise fixed wireless environment, there will be temporal changes in the response along a transmit-receive path, i.e., the static responses predicted using the a ray-tracing tool like WiSE will not suffice to fully characterize the channel. We can envision the full response on a given path as being the sum of a static one (e.g., one predicted using site-specific ray tracing) plus a zero-mean time-varying one, based on some type of empirical model. More specifically, the time-varying part can be thought of as a set of time-varying processes added to the rays of the static part.

Some questions that arise are: Which rays (or taps of the effective impulse response) will be time-varying? What will be the relative strengths, e.g., the

mean power of the time-varying part relative to the power of the static part? How will this ratio vary across taps? Can the time variations of the tap gains be modeled as random processes and, if so, what kind? How will the answers to these questions depend on the channel bandwidth, the specific site, the specific path, and the type of surrounding motion?

A full set of answers to these questions would lead to a highly useful model for the time-varying part of the wireless channel response. At the same time, acquiring these answers would take an extremely comprehensive measurement program spanning many environments, paths, motion scenarios and bandwidths. We have made numerous measurements, as we will report here, but not nearly enough to satisfy such requirements. Our less ambitious goal is to show, for some typical motion scenarios, that (1) only a few impulse response tap gains show significant variations; and (2) a well-known family of Gaussian random processes (the autoregressive processes, to be described later) can be used to characterize the time-varying nature of the tap gains. Since these findings apply across all the cases studied, we regard them as providing a highly useful starting point for time-variation modeling of indoor channels with fixed transmitter and receiver.

We defined four different kinds of motion scenarios-the static one (no motion) and three others-and we conducted a set of temporal measurements for each. Section 3.2 describes these specific motion categories and the associated experiments. Section 3.4 explains the use of random processes to describe these time variations. Section 3.5 demonstrates our methodology for identifying the appropriate process for each motion scenario. Section 3.6 summarizes our main findings.

3.2 Measured Environments

Static Environment

We placed the antennae in the ORBIT room 3.65 m apart and measured the channel response at $N = 1601$ frequencies between 3.0 and 4.0 GHz. We repeated the measurement $M = 100$ times, at 2-second intervals. During the experiment, no one was present in the room.

Quasi-Static Environment

We placed the antennae in the ORBIT room 7.9 m apart and measured the channel response at $N = 1601$ frequencies between 3.0 and 3.1 GHz. We repeated the measurement $M = 600$ times, at 2-second intervals. During the experiment, 10-15 people were sitting around a table placed between the antennae and were eating lunch. Though they were sitting most of the time, people were also coming or leaving from time to time, as would reflect a typical conference room scenario.

Random Movement

We placed the antennae in the ORBIT room 11.5 m apart and measured the channel response at $N = 401$ frequencies between 2.5 and 2.7 GHz. We repeated the measurement $M = 450$ times, at 2-second intervals. During the experiment, only one person was walking, running randomly between and around the antennae. There were no other people present in the room.

Office Space

This experiment was conducted in the office area of WINLAB. The receiver was placed near the door and the transmitter was placed at 10 m distance at a corner

across. We measured the channel between 3.0 and 3.1 GHz at $N = 1601$ equidistant frequencies. We repeated the measurement $M = 750$ times, at 2-second intervals. During the experiment, 10-15 people were sitting in their cubicles and walking in and out from time to time.

These experiments were conducted at different times as part of different projects at our laboratory. For that reason, the combination of N , M and bandwidth, W , was different for each of the four above scenarios. The point we make here is that, despite differences in (N, M, W) , the time variations of the tap gains for each category of people motion lend themselves to characterization by well-known random processes.

To study the four motion scenarios we defined and computed several quantities as follows: The total power gain (sum of squared magnitude of all impulse response components) is denoted by P_{trial} and is computed for each measurement (trial). The average of P_{trial} over the M measurements is denoted by P_{avr} . Departures of the set of P_{trial} values from P_{avr} reflect the temporal fluctuations of the ray (or tap) gains. The mean-square fluctuation of the n^{th} tap's squared magnitude about its average value is denoted by $\sigma_{tap}(n)$ or just σ_{tap} .

3.3 Time Variation in Measured Environments

3.3.1 Static Environment

In the static environment the channel response is nearly constant. P_{trial} deviates at most 1% from P_{avr} . The variations of the individual tap power gains are also negligible. σ_{tap} at the most variable tap corresponds to only 0.3% of P_{avr} . Since the variations among the trials are insignificant, the channel response measured for one trial suffices to describe the environment. This was the case for the experiments that produce Table 6.1.

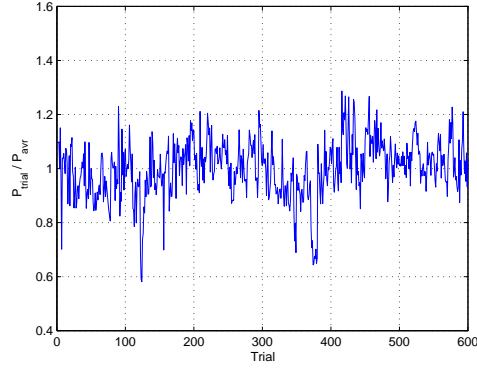


Figure 3.1: Ratio of the trial power gain P_{trial} to the average power gain P_{avr} versus trials (Quasi-Static Environment)

3.3.2 Quasi Static Environment

Fig. 3.1 shows the ratio of P_{trial} to P_{avr} in the quasi-static environment. P_{trial} varies at most 40% of P_{avr} . Fig. 3.2 shows σ_{tap} normalized by P_{avr} . Only four taps have σ_{tap}/P_{avr} greater than 2%. This 2% threshold is used for comparing different environments not for modeling purposes.

3.3.3 Random Movement

In this environment, P_{trial} deviates up to 20% from P_{avr} . The variation shows homogeneity, i.e., there are no trends or huge variations. Not all of the individual rays contribute to this variation in the same way. We plotted σ_{tap} , normalized by P_{avr} and saw that two taps contribute most to the variation of P_{avr} . All other taps have σ_{tap} less than 2% of P_{avr} variation in this environment.

The reasons that some of the tap gains show significant variation can be explained as follows. A moving object (e.g., a person or a clustered group of people) corresponds to one (or possible two) delay bins of the impulse response. The tap gain for each such delay bin will vary with time. For delays corresponding to non-moving objects, the tap gain will be essentially constant. The sets of time

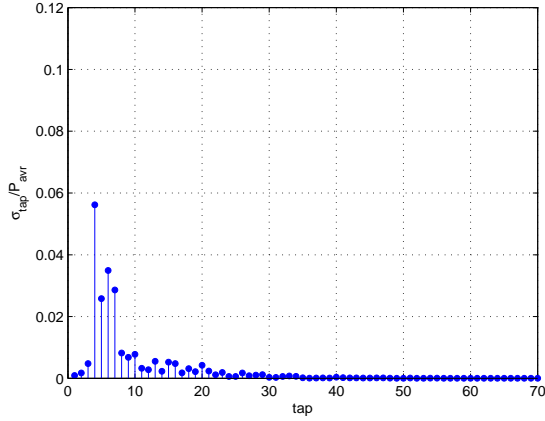


Figure 3.2: Ratio of the tap power gain to average power gain versus tap number (Quasi-Static Environment)

samples taken for the highly variable tap gains showed, in most cases, a reasonable conformity to a complex Gaussian distribution. This is likely due to the many returns from numerous scatterers (people), and the central limit theorem.

3.3.4 Office Space

In this environment, P_{trial} deviates up to 50% from P_{avr} . The variation has multiple means and slopes. We plotted the standard deviations of the tap power gains, σ_{tap} , normalized by P_{avr} , and saw that seven taps have normalized standard deviations greater than 2%.

3.4 Time Variation Modeling

3.4.1 Prior Work on Autoregressive Processes

Autoregressive processes have been used for spectrum estimation purposes [15] and for modeling the variation of the channel response across frequencies [16]. In [16], the authors showed that a second-order AR process is sufficient to model the

channel response across frequencies in a wideband indoor environment. Later, this approach was used in the ultra-wideband (UWB) channel modeling of indoor environments, [17]-[18]. A second-order AR process is proposed in [17] to capture the main characteristics of the UWB channel. In these studies, the frequency response is assumed to show insignificant change across time. To the best of our knowledge, autoregressive processes have not been used to characterize temporal variations of channel responses between fixed terminals.

3.4.2 Autoregressive Integrated Moving Average (ARIMA) Models of the Variations

We measure the complex channel response at N equally spaced frequency bins within a frequency range; we repeat this experiment M times within a time interval; and we define a matrix \mathbf{H} , where the entry in row i and column j corresponds to the complex channel response value at frequency f_i and trial t_j :

$$H(f_i, t_j) = \overline{H}(f_i) + \delta H(f_i, t_j) \quad i = 1 \dots N \quad j = 1 \dots M.$$

$\overline{H}(f_i)$ is the mean of the channel response over M time instants at frequency f_i ; $\delta H(f, t)$ is the time varying part; and we model $\delta H(f, t)$ through AR processes.

Specifically, we transform $\delta H(f, t)$ into the time domain and obtain $\delta h(n, t)$. The (complex) variation of $\delta h(n, t)$ at tap n across trials t constitutes a time series. We denote this time series as x , and we model it using ARIMA processes. We use the Box-Jenkins methodology, described in the Appendix, which also classifies the different members of the ARIMA family of processes.

3.5 ARIMA Modeling and Results

We now describe the modeling of x at a single tap in each environment. Models for the other significant taps can be found in a similar way. We will demonstrate

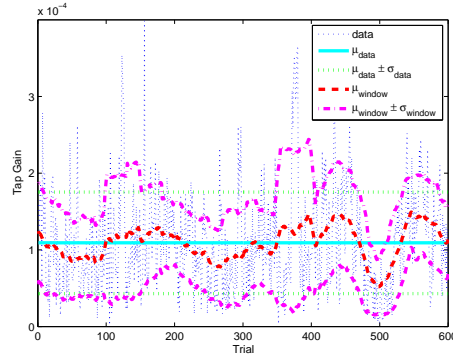


Figure 3.3: Mean and standard deviation (Quasi-Static Environment)

the Box-Jenkins methodology step by step as we find an appropriate model for the time variation in quasi-static environments. For the other environments, we will merely summarize the results.

3.5.1 Quasi-Static Case

Figure 3.2 shows that tap#4 is the most time-varying one in this case. We now model the discrete time series x for this tap.

Identification

Mean and Variance

A stationary time series has the window mean and standard deviation agreeing with the overall data mean and variance to a great extent. We compute local means and variances of the absolute tap gain shown in Fig. 3.3 using sliding windows of size 50. 50% of the window mean samples deviate from the data mean by at most 15% and 90% of the window mean samples are within 30% of the data mean. Also, 90% of the window standard deviation samples are within 30% of the data standard deviation. This data can be classified as statistically stationary.

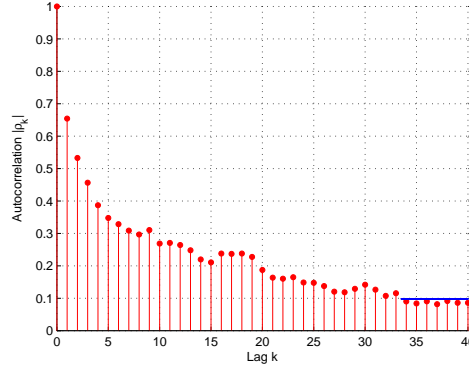


Figure 3.4: Auto Correlation Function (Quasi-Static Environment)

Auto Correlation Function (ACF)

For an MA process of order q the ACF is zero after the lag q . For an AR process it decays to zero exponentially or as a mixture of damped sine waves. Figure 3.4 shows the ACF of x . The horizontal lines at $\rho_k = \pm 0.0982$ show the zero thresholds computed using the Barlett approximation (Eq.(2.1.13) in [19]) which gives the variance of the estimated autocorrelation values ρ_k at lags beyond which the theoretical ACF may be deemed to have died out. The ACF decays exponentially and is effectively 0 after the lag 33.

Partial Correlation Function (PCF)

For a stationary process X , the partial autocorrelation at the k^{th} lag is the correlation coefficient between X_1 and X_{k+1} after eliminating the effect of X_2, \dots, X_k . For an AR process of order p , the PCF is zero after the lag p . Fig. 3.5 shows the PCF of x . The standard error σ of the estimated PCF values is approximately $1/\sqrt{n}$, where n is the number of samples. The horizontal 2σ lines are used as zero thresholds. The PCF is below the threshold after the third lag.

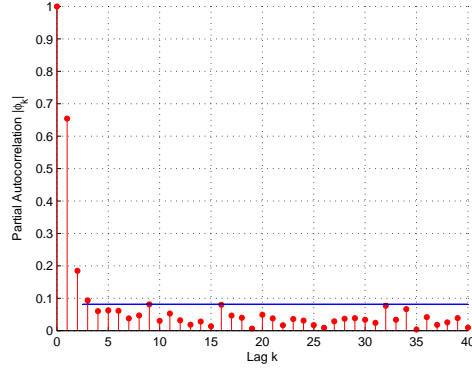


Figure 3.5: Partial Correlation Function (Quasi-Static Environment)

Choosing the possible models

Since the PCF is effectively zero after the third lag and the ACF tails off exponentially, we conclude that an AR(3) model is suitable. The value of PCF at the second lag is very small; therefore, the AR(2) model is also worth considering.

Estimating Parameters

We have estimated AR coefficients for the AR(2) and AR(3) models. The coefficients for the AR(2) model are $a_2(1) = 1.0000$, $a_2(2) = -0.5346 + 0.0249i$, $a_2(3) = -0.1833 - 0.0235i$. The coefficients for the AR(3) model are $a_3(1) = 1.0000$, $a_3(2) = -0.5175 + 0.0221i$, $a_3(3) = -0.1332 - 0.0228i$, $a_3(4) = -0.0934 + 0.0032i$.

Diagnostic Check

The AR(2) model and the AR(3) model in Fig. 3.6 show variations similar to those of the data. Choosing either one of them would not make much difference. For the cases where it is not so obvious which model is better, it is useful to have a criterion which indicates the appropriate model. We used the Akaike Information Criterion (AIC) to compare the models [20]. The AIC was derived by minimizing an information theoretic function, and it includes a penalty term

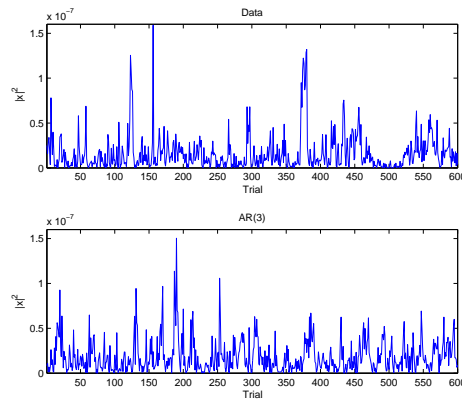


Figure 3.6: AR(3) process compared with data (Quasi-Static Environment)

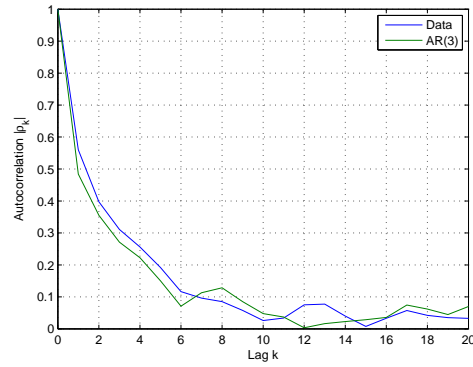


Figure 3.7: Comparison of autocorrelation function of the data and AR(3) process (Quasi-Static Environment)

for extra AR coefficients. The model which has the lowest AIC metric is chosen. In this case, the AIC was nearly the same for both models: For the AR(2) model, it was -15.68 , and for the AR(3) model, it was -15.69 . The comparison of autocorrelation functions the data x and of the AR(3) process is shown in Fig. 3.7. The autocorrelation function of the AR process has the similar decay as the data.

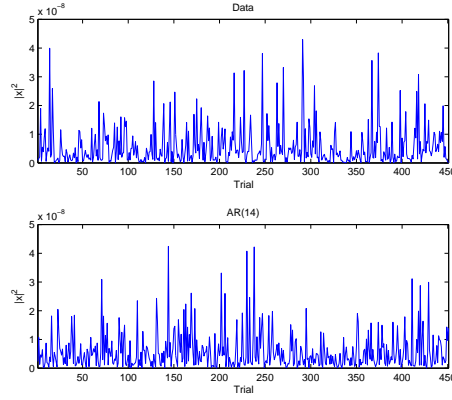


Figure 3.8: AR(14) process compared with data (Random Movement)

3.5.2 Random-Movement Case

Here, we modeled x at the third most varying tap. For this tap, 90% of the window mean samples deviate from the data mean by at most 18%. 90% of the window standard deviations are within 17% of the data standard deviation. Thus, the window mean and standard deviation agree to a great extent with the data mean and standard deviation, so the process is deemed to be stationary. The ACF in this case tails off as a mixture of exponential decays and damped sine waves and PCF is zero after the first tap. Fig. 3.8 shows AR(14) process which shows similar variations with the data.

3.5.3 Office Space

We modeled x at the most varying tap. The mean function in this case is not constant. Moreover, the all-pole model has poles outside the unit circle. Therefore, the process is not stationary. We applied a difference operator and investigated stationarity again.

To begin, we compared the window means and standard deviations with those for the first order difference ∇x . The local standard deviations were found to be

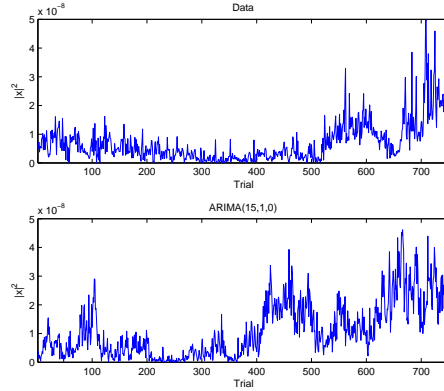


Figure 3.9: ARIMA(15,1,0) model compared with data (Office Space)

close to those for the data. The all-pole model now has all of the poles inside the unit circle. The window mean is close to zero, which is also the data mean. Therefore, the first order difference process ∇x is deemed to be stationary.

Next, we find an ARMA model for ∇x . The ACF of ∇x decays as a mixture tails off as a mixture of exponential decays and damped sine waves, and the PCF has an exponential-dominated decay. It is effectively zero after 11. lag. We choose ARIMA(15,1,0) process as shown in Fig. 3.9.

3.6 Conclusion

We have shown that the time variations of the channel response in an indoor environment are not negligible in common scenarios such as people sitting around a table or working in an office. We stochastically modeled the time variation of the channel response about the mean using members of the ARIMA family of processes and showed that this can lead to an accurate representation. Our key finding is that ARIMA processes are capable of describing the time variation of the impulse response terms in these environments. We obtained excellent agreement using such processes for each of the categories identified and measured.

Chapter 4

Emitter Localization and Visualization (ELVIS): A Backward Ray Tracing Algorithm for Locating Emitters

4.1 Introduction

Except for urban canyons, the localization problem for outdoor scenarios can be effectively solved by attaching GPS devices to the transmitters that need to be localized [21]. However, the reception of GPS signals is unreliable in most buildings. Therefore new technologies are needed to localize emitters inside buildings.

4.1.1 Prior Work

The various approaches in the literature for localizing first responders inside buildings can be broadly classified into three categories: TOA, AOA and signal-strength-based techniques [22] [23] [24]. These can be realized within the domain of existing networks and technologies such as, GSM networks [21], 802.11b networks [25], Bayesian-based localization or ultra-wideband (UWB) techniques.

4.1.2 Our Contributions

We propose a new algorithm, called ELVIS for localizing emitters based on backward ray tracing. Our work uses backward ray tracing for the first time for indoor

emitter location prediction. ELVIS combines TOA, AOA and signal-strength-based techniques with backward ray tracing into a single framework. One advantage of our algorithm is that three dimensional (3D) localization could be done even with one receiver.

We assume that each first responder carries a beacon emitting a signal of known characteristics. We locate such an emitter placed inside a building based on signals received by one or more receivers. The receivers measure received power as a function of AOA as well as TOA.

To assess the performance of ELVIS, it would be ideal to determine location based on data collected from high angular and temporal resolution receivers. As a preamble to making such measurements we estimate the localization accuracy based on synthetic data obtained from WISE (Wireless System Engineering), a forward ray tracing program, developed at Bell Labs [4].

As an application, we apply ELVIS to localize an emitter placed in the Bell Labs Crawford Hill building in Holmdel, NJ. We emulate this test environment using WISE. We specify the building blueprint, emitter position and transmit power, and WISE gives the received power, AOA etc. of all rays at any point in the building. We run ELVIS on this data and localize the emitter. As a practical matter, ELVIS would obtain its data from directional antennae placed at the receiver. Measurements collected using real receivers suffer from degraded accuracy because of finite angular and temporal resolution of the receivers. In addition, as ELVIS relies on using the blueprint of the building to estimate the location of the emitter; imperfect knowledge of the environment leads to errors in the amplitude of the arriving signals, perceived as "fading". Additive receiver noise is yet another source of error. We emulate such effects by perturbing the values given by WISE with errors due to fading, noise and finite resolution before running ELVIS.

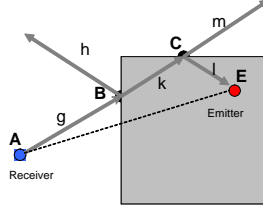


Figure 4.1: Backward ray tracing: Each ray becomes a new arrival at the effective point of incidence

4.2 WISE (Wireless System Engineering)

Given a building plan, transmitter and receiver locations, WISE measures radio-signal properties at any point in the building. WISE takes into account the layer properties of the walls. The reflection and transmission coefficients are determined based on the angle of incidence and layer properties at each interaction with a wall. WISE simulates the ray traces at the receiver as in Figure 4.2. The relevant output of WISE for generating ELVIS inputs is N received rays and their AOA's (both azimuth and elevation angles), powers and delays.

4.3 Backward Ray Tracing in ELVIS

In ELVIS, the N ray arrivals at the receiver which have the most received power are considered, with N chosen to reduce complexity without sacrificing performance. Each of these N rays is traced backward to the wall with which it last interacted. The reflected and transmitted rays are determined at the point of incidence, as shown in Figure 4.1. Backward ray tracing is applied until stopping conditions are reached or the ray leaves the building. The same concept is applied for other arrivals to determine candidate intersection points, one of which could be a true emitter location. For backward ray tracing, we have to determine if the ray hits a wall and if so, where. In [26] we discuss this problem in detail and derive conditions for the 3D case.

4.4 Emulating Degradations

We treat the case of ideal conditions (no other objects, perfectly-known blueprint and materials), but we also treat the departures from ideal. We assume, initially, that each receiver makes perfect measurements of time delays, arrival angles and ray amplitudes. To obtain realistic assessments, however, we then relax these assumptions by considering finite resolutions in delay and angles, and signal fading plus noise. Our paper [26] discusses in detail how we emulate these degradations.

4.5 ELVIS

4.5.1 Basic Algorithm

ELVIS consists of three steps:

1. *Backward ray tracing* - For each arrival, we apply the backward ray tracing method separately. We save all backward-traced rays along with their powers and propagation delays. We stop backward ray tracing if any of the stopping conditions occur.
2. *Determining candidate locations* - Candidate locations are pairwise intersections of the back-traced rays. Under ideal conditions, emitter location is characterized by having multiple ray intersections with all backward ray traced powers equal to each other and to P_T and with the same generation times.
3. *Choosing the actual source location* - As there are usually multiple candidate locations, there is a need to establish metrics for choosing the most likely one. We consider the following metrics:
 - (a) *Number of intersections in the vicinity*: The regions with multiple candidate locations are more likely to contain the emitter location

therefore the candidate locations in these areas have higher metric.

- (b) *Predicted power difference between rays:* At the true emitter location the predicted powers of intersecting rays are expected to be equal.
- (c) *Power difference between the expected transmit power P_T and predicted power P for each intersecting ray:* At the emitter location the predicted and estimated power should be equal.
- (d) *Relative delay between arrivals:* ELVIS does not depend on the arrival times of the rays. However, we assume the receiver is able to estimate delay differences among arriving rays. ELVIS can also estimate these arrival times for any given candidate location. Thus, the set of relative delays measured by the receiver can be compared against the set of relative delays computed for any candidate location. The difference comprises another metric.

The metrics can be weighted differently depending on the reliability of the measurement. The candidate location which has the highest metric sum is chosen. In this work, we weight the metrics equally. The metrics are explained in mathematical detail in [26].

4.5.2 Multiple Receivers

Each receiver sends to the central processing unit the AOA of each incoming ray, TOA, received power and the coordinates of the receiver. The ELVIS algorithm for multiple receivers is the same as for the single receiver case, except for the ray selection. We select the N strongest (in terms of received power) rays received among all antennas.

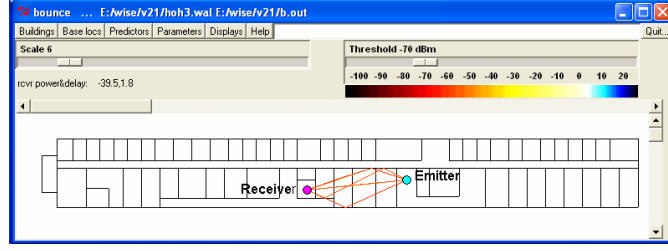


Figure 4.2: WISE output: Radio paths between receiver and emitter in the Crawford Hill building. This building is about 120 m x15 m

4.6 Simulation results

For investigation of the overall performance in the whole Crawford Hill building, we fixed the location of the receivers and varied the location of the emitter among 72 sample locations uniformly distributed in the building. We have computed for each sample point the location error, i.e. the distance between predicted and true emitter location and determined the CDF (Cumulative Distribution Function). We chose $N = 5$ as a tradeoff between computational complexity and accuracy in our simulations.

4.6.1 Perfect Measurements

First, we assume the receiver is able to resolve rays with exact measurements of angle, delay and power.

Single Receiver

Figure 4.3 shows the CDF of the location error using a single receiver. We see that, for 90% of the building, the location error is less than 2 cm with a maximum error of 9 cm.

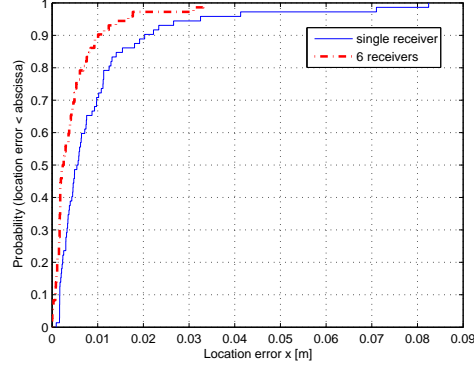


Figure 4.3: CDF of Prediction Error by perfect measurement of power, TOA and AOA

Multiple Receivers

Figure 4.3 also shows the CDF of the location error using 6 receivers, which are placed both inside and outside the building. We could localize over 90% of the building within 1 cm using multiple receivers, with a maximum error of 3.5 cm.

4.6.2 Degraded Measurements

For angular degradation, we quantized the elevation and azimuth angles using 0, 10 and 20 degree quantization bins. For the temporal degradation, we quantized the TOA's of the rays using 0, 10, and 20 ns bins. We also distorted the signal amplitude to emulate fading and added noise to the measurements. In the following CDF's, N denotes degradation due to noise, F+N denotes degradation due to fading and noise and 10 ns-20 ns denote the width of the quantization bin for degradation of TOA.

Single Receiver

We compared the CDF of location error for various degradations, assuming perfect measurement of the AOA. In the noise-only case, we can localize an emitter within 5 m over 93% of the building. Adding fading to the signal amplitude, we can

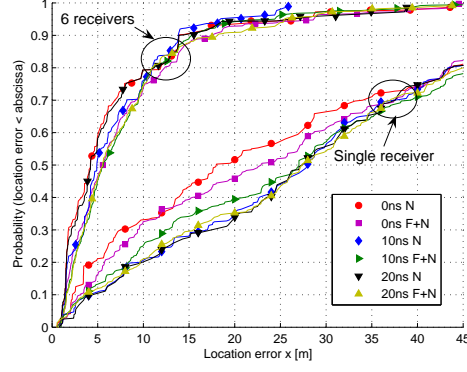


Figure 4.4: CDF of Prediction Error using 20 degree angular bins and various degradations

localize over only 75% of the building within 5 m over. Figure 4.4 shows that setting angular quantization bins to 20 degrees, we can localize within 5 m over only 10 – 20% of the building.

Multiple Receivers

Using 6 receivers and having perfect angular resolution, the location errors are within 5 m over 90% of the building at worst. For bins of 20-degree width, Figure 4.4 shows that location error within 5 m occur over only 48% of the building and 10 m occur over 80%. Also the spread over different cases (N, F+N, etc.) is smaller with multiple receivers.

4.7 Conclusion

We have developed and simulated ELVIS, a backward ray tracing-based localization tool for indoor environments. We have determined that backward ray tracing can be effective even with degradations, especially if multiple receivers are used. We find that, if the angular resolution is high, ELVIS gives reliable results with a single receiver. At lower angular resolution, multiple receivers are necessary to localize with good accuracy. Fading and noise are not major causes

of degradation in most cases of interest.

We have simulated the measurements at the receiver using WISE. Further work could include (1) investigation of other metrics, to improve the performance; (2) investigation of the performance in other buildings; (3) adding other error sources, such as uncertainties in the blueprint and wall properties; and (4) verification of this technique through measurements.

While we find that the backward ray tracing technique in ELVIS produces highly accurate results using ideally accurate measurements, finite angular resolution is the primary source of degradation in accuracy. In the approach taken here the rays are traced back in the direction of the center of the angular bin on which they were received. Finite angular resolution can lead to rays being back-traced in wrong directions. With increased distance such rays may begin striking wrong walls and take paths that are not even in the same area as the transmitter. A possible remedy for this would be to back-trace multiple rays within each angular bin, allowing better candidate locations to be discovered.

Chapter 5

An Empirically Based Path Loss Model for Wireless Channels in Indoor Environments

5.1 Introduction

We present a statistical path loss model derived from simulated data with a ray tracing tool. We collected simulated data in four buildings. The characterization used is a nonlinear curve fitting of the decibel path loss to the decibel distance, with a Gaussian random variation about that curve due to the shadow fading. The transmission losses across the walls makes the linear models inappropriate for indoor scenarios. We model the transmission losses across the walls with an additional exponential term whose parameters show variation from building to building.

5.2 Data Collection

We predicted the received power in four different buildings using WISE at multiple transmitter-receiver locations. In this chapter we use this data for analyzing a new path loss model for indoor environments. In all of our simulations we set the the receiver and transmitter antenna heights to 2 m and set the frequency at 2 Ghz.

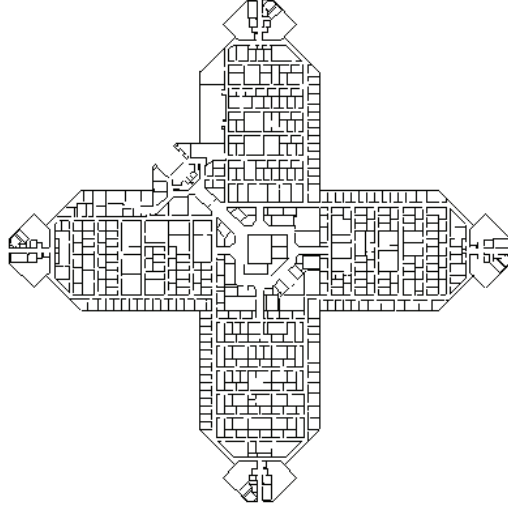


Figure 5.1: Building plan of AT&T Middletown Building

5.2.1 WISE Simulations for AT&T Building in Middletown, NJ

Figure 5.1 shows the AT&T Building plan in Middletown. It is 200-m long in each direction. We have chosen 175 transmitter locations uniformly distributed in the building 10 m distant from each other. For each of these transmitter locations we predicted received power with WISE at 14093 receiver locations. The receiver locations are uniformly distributed in the building with 1-m separations.

5.2.2 WISE Simulations for the Hynes Convention Center in Boston, MA

Figure 5.2 shows the the building plan of the Hynes Convention Center. It is a building of size 190 m x 140 m with large rooms. We have chosen 229 transmitter locations uniformly distributed in the building 10 m distant from each other. For each of these transmitter locations we predicted received power with WISE at 20331 receiver locations. The receiver locations are uniformly distributed in the

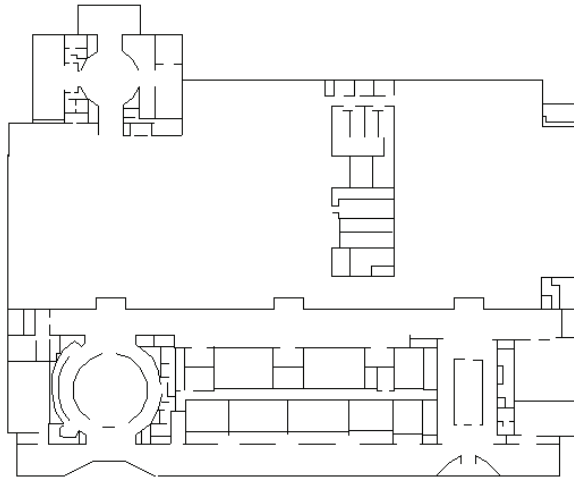


Figure 5.2: Building plan of Hynes Convention Center in Boston

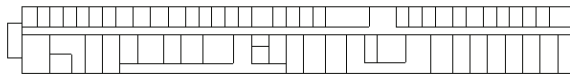


Figure 5.3: Building plan of Crawford Hill Building

building with 1-m separations.

5.2.3 WISE Simulations for the Alcatel-Lucent Building in Holmdel, NJ

Figure 5.3 shows the plan for this building (also called Crawford Hill Lab). It is a building of size 120 m x 15 m . We have chosen 24 transmitter locations uniformly distributed in the building with 10-m separations. For each of these transmitter locations we predicted received power with WISE at 162266 receiver locations. The receiver locations are uniformly distributed in the building with 0.1-m separations.

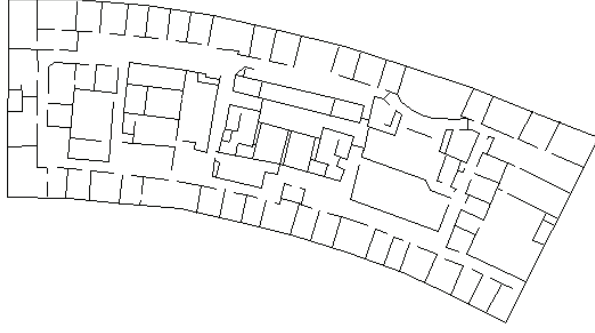


Figure 5.4: Curved office Building

5.2.4 WISE Simulations for a Curved Office Building

Figure 5.4 shows the the plan for a curved building of size 90 m x 14 m. We have chosen 37 transmitter locations uniformly distributed in the building 10 m distant from each other. For each of these transmitter locations we predicted received power with WISE at 9813 receiver locations. The receiver locations are uniformly distributed in the building with 0.5-m separations.

5.3 Path Loss Model and Results

The scatter plot of path loss and distance is shown in Fig. 5.5 for the data collected in the Curved Office Building. In this figure the circles correspond to the means of the sample path loss values in each 0.1-dB-wide distance bin. Unlike Fig. 1 in [27], which shows the scatter plot of path loss and distance for a macrocell in the Seattle environment, a linear regression alone is not appropriate in an indoor environment. We see that the bin averages follow a nonlinear shape as the distance increases. An explanation for this would be the effect of the transmission losses through the walls, which gets much more significant as the receiver is located further from the transmitter.

The transmission losses are parameterized as:

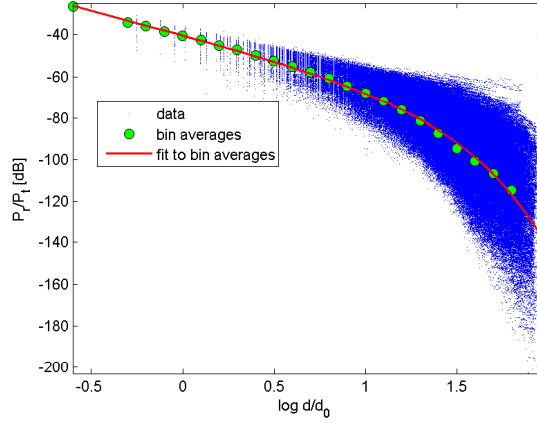


Figure 5.5: Path Loss versus distance

$$T = 10 \log e^{-\alpha d/d_0} \quad (5.1)$$

where α is a constant, d is the distance and d_0 is the normalization factor for the distance, i.e., a convenient ‘reference distance’. We set $d_0 = 1m$. (5.1) can be written as:

$$T = C \exp(\log(d/d_0)/\log e) \quad (5.2)$$

where $C = -10\alpha/\log e$. We extended the pathloss model in [27] by adding the term T in (5.3). We found that, the fit to bin averages follow can be parameterized as:

$$PL = A + B \log d + C \exp(\log(d/d_0)/\log e) \quad (5.3)$$

where A , B , C are the parameters.

Figure 5.5 shows the curve fit according to this parametrization. In the other buildings we investigated we found similar tendency as in Fig. 5.5. We clustered the path loss samples per 0.1-dB-wide distance bin and computed the mean and the standard deviation in each bin. Figure 5.6 show the variation of bin averages in each of these building, and Fig. 5.7 show the corresponding curve fits. Comparing Fig. 5.6 with Fig. 5.7 we see that the parametrization is capable of modeling the

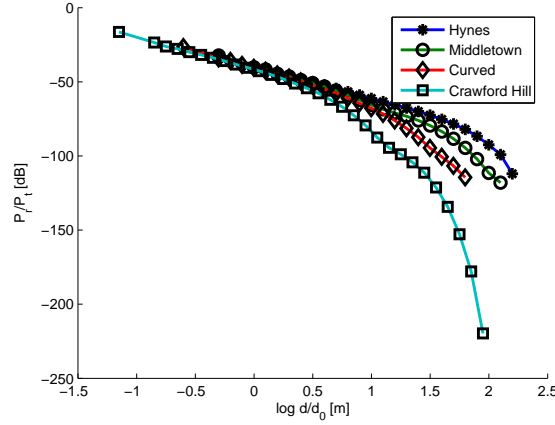


Figure 5.6: Sample means of the path loss values in each distance bin

nonlinear decrease of pathloss. Figure 5.8 shows the standard deviations about the mean path loss curves per 0.1-dB-wide distance bin for each building. The standard deviation increases with the transmitter receiver locations and each building show different variation of standard deviation with distance.

The CDF of the shadow fading component (dB variation of the path loss samples around the parameterized curve) for the Curved Office Building is shown in Fig. 5.9. In this figure a straight line denotes a Gaussian distribution. Therefore, we conclude that the variation of the path loss samples around the mean is log-normal if we consider the data collected from multiple receiver and transmitter locations together. We found similar results for the other buildings we considered. The parameters A , B , C are building specific. The specific values for each building we considered are given in Table 6.1. These are composite values over all Tx locations. We may want to do this differently.

We compared for the Crawford Hill Building the path loss model in (5.3) containing A , B , C terms with the conventional linear path loss model containing only the A and B terms. Figure 5.10 shows the standard deviations versus distance from the transmitter for both path loss modeling approaches. The stand

deviations from the linear fit considering only A and B is much higher than the standard deviation from the exponential fit with parameters A, B, C. For indoor path loss modeling, this emphasizes the value of adding the exponential C term to the conventional path loss model. The linear path loss model with only A, B terms does not adequately model large indoor environments where transmission losses gain much more importance with increasing distance.

5.4 Conclusions

Our modeling approach for indoor path loss using ray-tracing can find several useful applications. For example, a system planner can infer overall channel characteristics in a specific building. This path loss model could be used for testing the performance of the algorithms for deploying wireless systems in indoor environments. Instead of testing an algorithm in multiple buildings by doing extensive measurements or simulations, the performance can be evaluated by varying the parameters of the path loss model. Determining ranges of the parameters which correspond to the realistic buildings bears further study. Another application could be the use of WISE for a specified building for each of the N base location, which are in the order of 8-12, to find the parameters of the path loss model. That way, system planners can determine where to put bases to cover the area for a given system, and they do not have to store millions of data points, just a relatively small number of parameters.

Table 5.1: Parameters of the Path Loss Model

Building	A	B	C
Hynes	-40.16	-18.04	-0.18
Middletown	-39.52	-21.92	-0.26
Curved	-39.82	-22.79	-0.57
Crawford Hill	-41.71	-22.69	-1.39

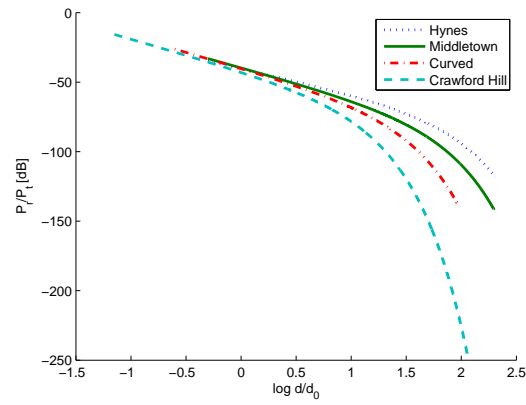


Figure 5.7: Curve fits to the mean curves in Fig. 5.6

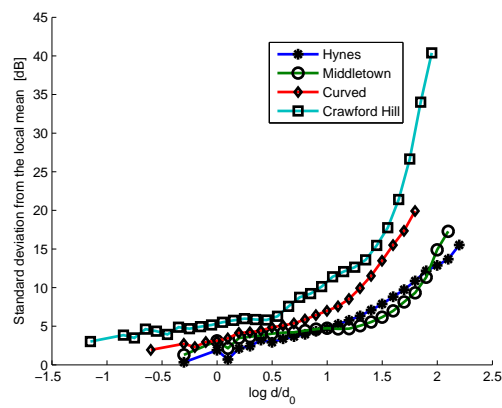


Figure 5.8: Standard deviations about the mean path loss curves

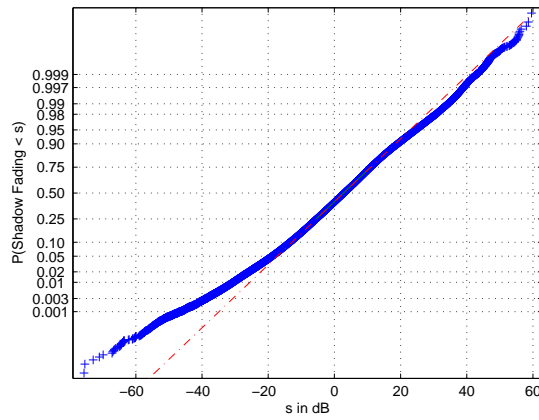


Figure 5.9: CDF of the shadow fading component for the curved office building. A straight line denotes Gaussian distribution. This case is typical for the other buildings we considered.

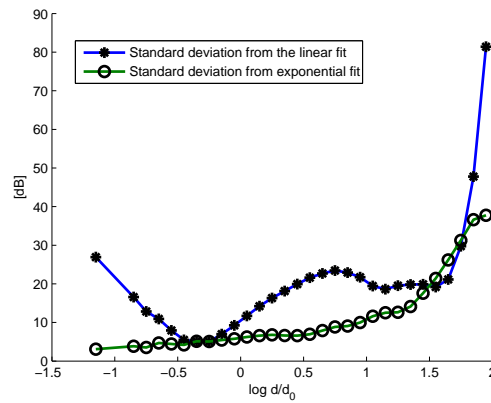


Figure 5.10: Comparison of standard deviations from the linear fit using the conventional path loss model with the standard deviations from the exponential fit in (5.3) for the Crawford Hill Building

Chapter 6

Calculating MIMO Performance in Urban Microcells Using Ray-Tracing

6.1 Introduction

The focus of our study is on urban area with a dense user population. We assume this area is served by microcells with small, low-cost base stations; and that, to maximize throughput and reliability, the links use multiple-input/multiple-output (MIMO) techniques. A challenge in the evaluation of such a system is to realistically capture the spatial variation of the channel gain matrix along a path and throughout an area. MIMO techniques exploit the uncorrelated spatial channels offered by wireless multipath to improve reliability and throughput. The frequent assumption in modeling the channel is that the elements of the channel gain matrix are complex Gaussian (Rayleigh fading) and the correlations are zero; or there is a non-zero K-factor and a specified correlation matrix [28]. There are also physical stochastic models which model clusters of scatters in the environment geometrically [29] or describe the paths between the transmitter and receiver locations by statistical parameters only [30], [31]. In using a purely stochastic model, one is essentially modeling the channel gain matrix, in particular, the average path gain; the fading statistics of the individual path gain matrices; and the correlations among them [32], [33], [34], [35].

Stochastic models require many assumptions about the fading statistics; even when they are accurate, it is not easy to model the channel gain matrix as it

varies along a specific path. We present an evaluation approach for narrowband-MIMO systems where the location-specific and time varying nature of MIMO channel gains is simulated via an environment simulator based on ray tracing and site-map. By using such a simulator in specific environments, neither the sets of assumptions for stochastic modeling nor long measurement campaigns [36] are needed. We determine the actual channel gain matrix at closely-spaced discrete positions of the terminal as it moves through a given environment. This permits us to compute performance for a specific Tx-Rx link, or a specific Tx location and Rx trajectory.

For urban microcell environments [5] and [6] show very good agreement between the signal strength (or path loss) statistics of environment simulators based on ray-tracing and those from extensive measurements. In [5] the comparisons are done for data collected in Manhattan and Boston, and in [6] the comparisons are done for data collected in a two-square kilometer area of Rosslyn, Washington DC. The comparisons show that ray-tracing based simulators can predict signal strengths in these outdoor environments with very good accuracy.

A ray-tracing approach for location-specific performance was also reported in [37], wherein bit-error-rate performance was determined for specific trajectories and terminal speeds in urban microcells for single-antenna links. Here, we do something similar, only for throughput on MIMO links. Specifically, we simulate MIMO channels in Manhattan and Boston, for many paths in each city. In all scenarios, we consider the movement of mobiles along streets and compute the channel gain matrix, capacity and throughput versus position. We also obtain the cumulative distribution functions (CDF) of these metrics over the paths traversed.

Section 6.2 compares performance for MIMO configurations with vertical and horizontal array orientations; different array combinations (3x1, 2x2, 4x2, 3x3, 4x4); varying antenna heights; two antenna types (dipole, isotropic); two polarizations (vertical, horizontal); and four MIMO transmissions schemes (Water-filling,

Spatial Multiplexing, Beamforming, Double Space Time Transmit Diversity (D-STTD) [38]). We also compare MIMO performance with that for single-antenna links. Finally, we compare, for both line-of-sight (LOS) and non-line-of-sight (NLOS) paths, the CDFs derived using the ray-tracing emulator with those predicted using a familiar stochastic model, i.e., i.i.d. Rayleigh fading gain matrices.

On paths where none of the practical MIMO transmission modes is superior to all others over an entire path, adapting the MIMO transmission mode to the varying channel conditions allows additional gains. In Section 6.3, we propose practical methods of mode adaptation. In each scheme, the transmitter switches between diversity and spatial multiplexing modes to achieve good data rates as the mobile moves.

In Section 6.4, we consider multiple MIMO base stations to cover a full urban neighborhood and investigate co-channel interference (CCI) and achievable rates. We use binary integer programming to solve for the minimum number of base stations needed such that received SNR throughout the desired coverage area is above a specified threshold. We then evaluate different possible frequency reuse plans and compare them in terms of achievable rate.

6.2 Location-Specific MIMO Performance in Urban Wireless Channels

6.2.1 Motivation

We devise an evaluation approach for wireless systems using MIMO links wherein the location-specific channel gains are determined for actual path geometries. Specifically, we simulate the channel gain matrices along various paths in Boston and Manhattan using a versatile and accurate ray-tracing tool. We compare and quantify the performance of MIMO systems for various transmission schemes

(spatial multiplexing, beamforming, space-time transmit diversity) and antenna configurations (array size, array orientation, element pattern, polarization and height). Our performance metric is the CDF of throughput for users moving along streets. We compare, for both line-of-sight and non-line-of-sight paths, the CDFs derived using the ray-tracing emulator with those predicted using a familiar stochastic model, i.e., i.i.d. Rayleigh fading gain matrices.

6.2.2 Simulation Method

We use ray tracing to simulate the MIMO channel gain matrices, and also the single-antenna channel gain, for a fixed base (transmitter) and varying mobile (receiver) locations along a path. We predict the complex channel gain matrix, \mathbf{H} , in 5-cm steps along every path we considered. To compute the noise variance, we assume a noise figure of 10 dB and a noise bandwidth of 5 MHz. Unless otherwise noted, the total transmit power is 10 dBm; the center frequency is 2.4 GHz; and the base and mobile antenna heights are 10 m and 2 m, respectively. Antenna elements are placed on a uniform linear array on both sides of a link.

Using blueprints (site maps) for Boston and Manhattan, we did simulations for 14 different paths on various streets in both cities. Figure 6.1 shows three sample paths among the 14 paths we considered: 1) a 274-m LOS path on Park Avenue in Manhattan between 48th and 52nd Streets, where the transmitter is fixed at A and the receiver moves from P1 to P2 2) A 323-m long path on Lexington Avenue in Manhattan, between 100th and 105th Streets, where the transmitter is fixed at B and the receiver moves from P3 to P4 3) A 50-m NLOS path on the 103rd Street, where the transmitter is fixed at B and the receiver moves from P5 to P6.

The ray-tracing tool we use is WiSE, a software program developed by Bell Labs that is capable of capturing the realism of many radio approaches and environments [?]. At each receiver position, WiSE computes the complex receive rays and can deliver both the sum of ray powers and their complex ray sum (vector

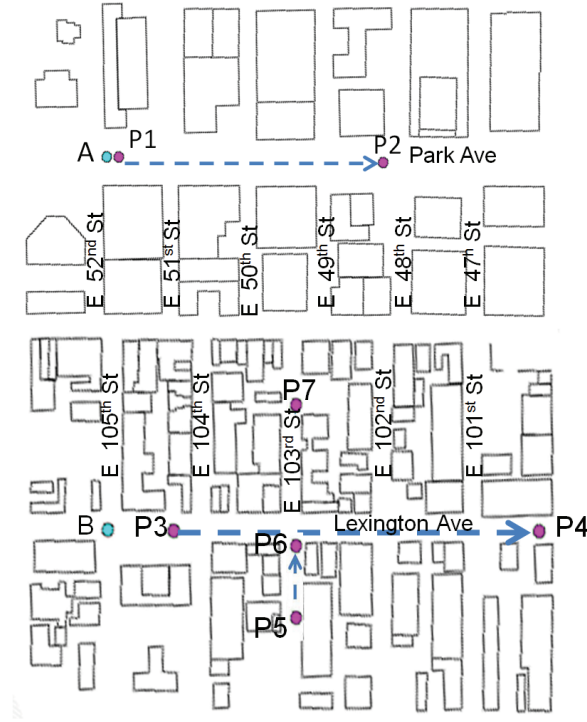


Figure 6.1: Street plan in Manhattan. Three paths are shown: 1) The transmitter is fixed at A and the receiver moves from P1 to P2, a 274-m LOS path on Park Avenue. 2) The transmitter is fixed at B and the receiver moves from P3 to P4, a 323-m LOS-path on Lexington Avenue. 3) The transmitter is fixed at B and the receiver moves from P5 to P6, a 50-m NLOS-path on East 103rd Street.

sum) at a particular frequency. In this study, we primarily use the vector sum, so as to obtain a gain matrix, \mathbf{H} , under a narrowband signaling assumption.

Unless otherwise specified, we will show results for capacity, using standard formulas from the literature [39]. In some cases, however, we will show results for achievable data rate (throughput) for alternative MIMO transmission modes, such as beamforming and space-time coding.

6.2.3 Results

We now present graphical results for some of the many cases we considered, both for the specific paths shown in Fig. 6.1 and for the other paths in the two cities.

Our primary aim is to quantify the impact of the many design parameters that determine throughput performance. In addition, we examine various modes of system evaluation, including different features of the ray-tracing tool and the use of stochastic models, to see how sensitive our performance estimates are to the evaluation method.

Array Size and Transmit Power

We compared CDFs of capacity for single antenna, 2x2, 3x1, 4x2 and 4x4 links for the path P1-P2 shown in Fig. 6.1 along the Park Avenue. The average capacity for 4x4 MIMO is 80% greater than the average capacity for 2x2 MIMO, less than a 2:1 increase. Similarly, 2x2 MIMO yields only 65% more average capacity than a single-antenna system. A 3x1 MIMO system increases the average capacity by 19% over a single antenna system, as a result of added diversity. Similarly, the average capacity for 4x2 MIMO is 21% higher than the average capacity for 2x2 MIMO. Finally, average capacity increases roughly linearly with dB-transmit power. This is consistent with the capacity equation, wherein capacity is roughly proportional to the logarithm of SNR.

Polarization

Figure 6.2 compares CDFs of capacity for 4x4 MIMO using dipole antennas with vertical and horizontal polarizations and also using isotropic antennas. Using vertically polarized dipoles yields the more capacity than using horizontally polarized dipoles: It yields 7.3 bits/s/Hz more average capacity than use of horizontally-polarized dipoles, which corresponds to a 31% increase; and use of isotropic antennas yields additional 3 bits/s/Hz average capacity, which corresponds to a 10% increase compared to vertically polarized dipoles.

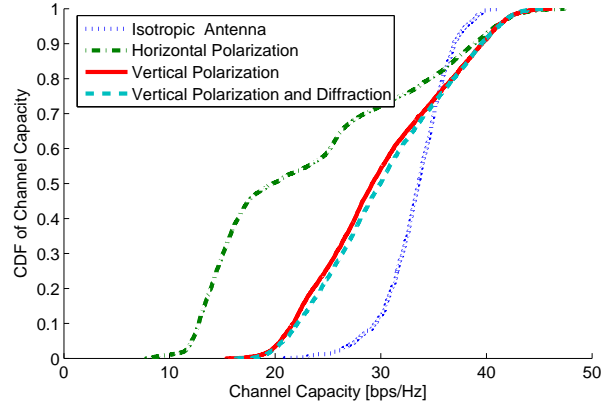


Figure 6.2: CDFs of capacity for 4x4 MIMO for various polarization types along the Park Avenue path in Fig. 6.1. Use of vertically polarized dipoles yield more capacity than the horizontally-polarized dipoles. Including diffraction effects does not change the CDF perceptibly.

Diffraction

Figure 6.2 also compares capacity CDFs, for the case of vertically polarized dipoles, both with and without diffraction effects considered in the ray-tracing tool. Including diffraction effects in the simulation increases accuracy but also running time, so it is valuable to see how much it matters. For the LOS path along Park Avenue in Fig. 6.1 the predicted capacity CDF does not change perceptibly. Here, the buildings on the both sides of the road have heights from 20-m up to 217-m and they are much wider than the buildings along Lexington Avenue. For the NLOS path P5-P6 on the East 103rd including diffraction effects increases the predicted average capacity by 0.7 bps/Hz. For the LOS path on Lexington Avenue Fig. 6.1, including diffraction effects increases the predicted average capacity by 0.4 bps/Hz and the CDF is (very) slightly different, as seen in Fig. 6.3.

For a 20-m long NLOS path in Boston the effect of including the diffraction is to increase the predicted average capacity by 2 bps/Hz. The CDFs for this case, seen in Fig. 6.3, clearly differ. At some specific locations along this path,

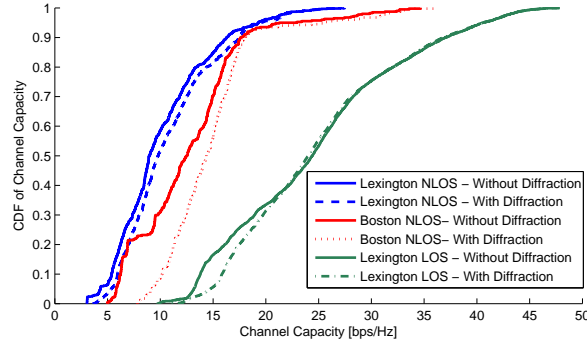


Figure 6.3: CDFs of capacity for 4x4 MIMO with vertically polarized dipole antennas, both with and without diffraction effects considered for the LOS path P1-P2 along Lexington Avenue, for the NLOS path P3-P4 on the East 103rd Street in Fig. 6.1 and for a 20-m NLOS path in Boston. The CDFs are only slightly different on the paths P1-P2 and P3-P4. On a NLOS path in Boston diffraction has more effect on the paths in Fig. 6.1.

the difference was as much as 9.3 bps/Hz. What we conclude is that diffraction effects are of minor consequence for paths that are essentially LOS, but should be included (the increased running times notwithstanding) in simulating NLOS paths or locations with lower received power.

Array Orientation

Figure 6.4 shows the CDFs of capacity for 4x4 MIMO with vertically polarized dipole antennas for two array orientations on the Park Avenue path in Fig. 6.1. Use of horizontally oriented arrays yields 12 bps/Hz greater average capacity, corresponding to a 68% improvement over using vertical arrays. We repeated this experiment comparing vertical arrays with horizontally polarized dipole antennas and horizontal arrays with vertically polarized dipole antennas. Use of horizontally oriented arrays with vertically polarized dipole antennas yield 62% improvement over using vertical array with with horizontally polarized dipole antennas. The implication of this significant difference is that most angular spread among multipath echoes occurs in the azimuth plane, not the elevation plane.

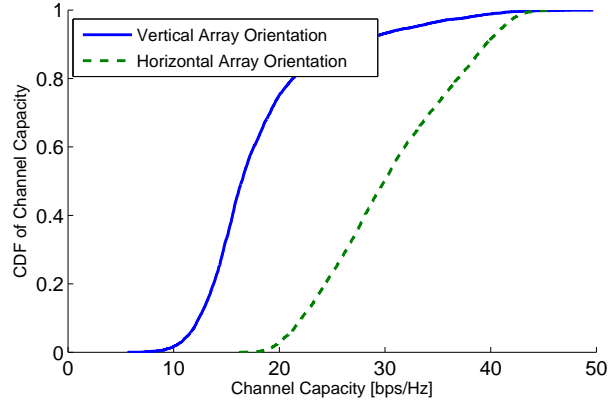


Figure 6.4: CDFs of capacity, for horizontally and vertically oriented arrays, for the Park Avenue path in Fig. 6.1. Use of horizontally oriented arrays yields an average capacity increase of 11 bps/Hz, corresponding to a 68 % improvement over using vertical arrays.

Antenna Height

For the Park Avenue path in Fig. 6.1, we kept the receiver antenna height at 2 m and, for a 4x4 MIMO array, we varied the base antenna height among the four values 2 m, 10 m, 20 m and 30 m.

Figure 6.5 indicates that, overall, the highest capacities are obtained for a 2-m base antenna height. For LOS paths like this, we find in general that, if the base-mobile ground separation is less than 200-m, a base height equal to that of the mobile antenna yields the highest average capacity. This is due to the minimum, for equal antenna heights and given base-mobile separation, in the geometric distance between base and mobile antennas, leading to lower path loss and thus greater received SNR. This effect is stronger when the mobile location is closer to that of the base, and it diminishes as the mobile moves farther along the path. Therefore, for large base-mobile ground separations the base height does not have much effect on the capacity.

It is important to note that our ray-tracing channel emulator does not take account of the obstacles along a street, such as buses, trucks and vehicles in

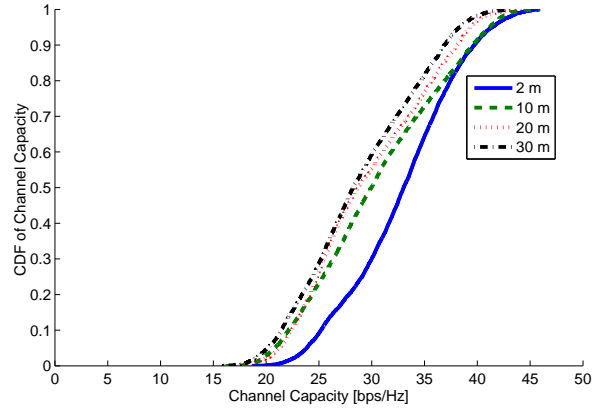


Figure 6.5: The highest average capacity is obtained when the transmitter and receiver antennas are at the same height.

general. Therefore, setting the base height at 2 m in our comparisons yields capacity results that are probably optimistic. In a realistic scenario, the base height would be set at 10 m or more, to minimize ground clutter.

Approach Based on Rayleigh Fading

For all its virtues, site-specific ray-tracing for complex environments like urban streets can require very long running times. An alternative approach we will consider here is as follows: (1) Use the ray-tracing tool for the same base positions and mobile paths we have considered so far. (2) For each receiver position, compute the total power sum-of-rays, rather than the vector sum-of-rays for each MIMO path, leading to an average path gain for each position; (3) assume that the underlying MIMO gain matrix, given that average path gain, is made up of i.i.d complex Gaussian elements as is assumed in many MIMO analyses; and (4) use that stochastic assumption to analyze the various MIMO modes for the various base-mobile paths considered.

We compared this approach with the more rigorous one of computing complex responses for each MIMO path for each receiver position. For example, Fig. 6.6

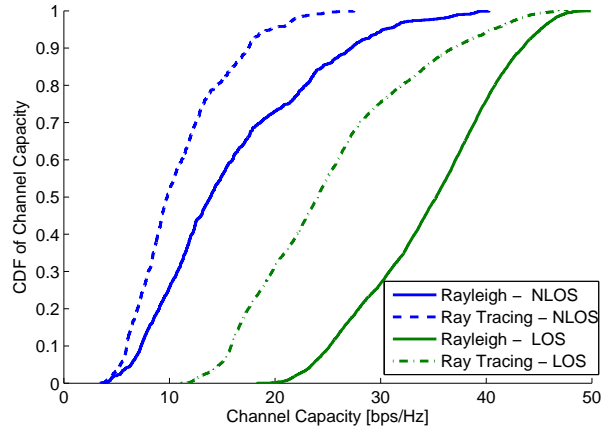


Figure 6.6: CDF of capacity for 4x4 MIMO on the LOS-path along Lexington Ave and along the NLOS path along 103rd street in Fig. 6.1. The dashed curve is obtained from H-matrices predicted via ray tracing; the solid curve corresponds to assuming Rayleigh channel gain matrices. The Rayleigh assumption is wildly optimistic and unreliable way for estimating performance on LOS paths. On the NLOS path, the CDFs have much better agreement than on the LOS path.

shows CDFs of capacity for 4x4 MIMO along the LOS path on Lexington Avenue and along the NLOS path on East 103rd Street, in Fig. 6.1. On both paths, the Rayleigh fading assumption leads to better statistics, because it results in gain matrices of full rank. However, there is a clear difference between the two approaches. For the LOS path, Rayleigh assumption is wildly optimistic and an unreliable way to estimate performance. The CDFs for the NLOS path, on the other hand, show much better agreement, no doubt due to the greater amount of scatter and multipath mixing for NLOS paths.

Different Cities and Neighborhoods

Figure 6.7 shows CDFs of capacity on five different paths at varying neighborhoods of Boston and Manhattan. LOS paths in Boston and Manhattan have higher average capacities than the NLOS paths.

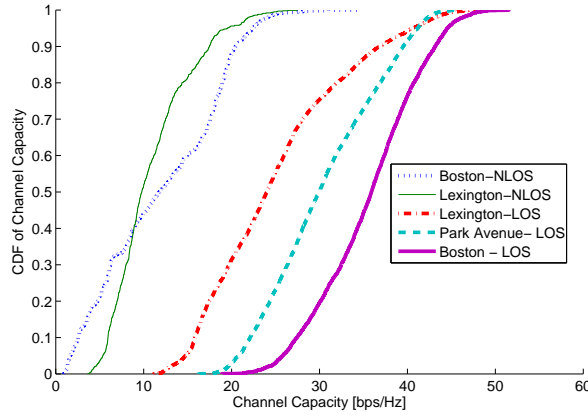


Figure 6.7: CDF of capacity for five different paths at varying neighborhoods both in Boston and Manhattan

Transmission Scheme

Figure 6.8 shows the maximum attainable data rate (throughput) versus distance on the Lexington Avenue path, P3-P4, in Fig. 6.1, for each of four possible transmission modes: water-filling, spatial multiplexing (SM), beamforming (BF) and D-STTD. Water-filling achieves the channel capacity, by means of its using optimal power allocation. If the channel is not known at the transmitter, the best strategy is to allocate equal power to each antenna; this is the case we refer to here as spatial multiplexing. In MIMO beamforming, the total power is allocated to the strongest eigenmode. Finally, D-STTD is a transmission scheme with two parallel 2x2 Alamouti transmissions; this is another version of 4x4 MIMO, which achieves both diversity and spatial multiplexing gains.

We assumed vertically polarized dipole antennas and included diffraction effects to simulate the 4x4 channel gain matrix along this path. We see that, in this case, SM is the best transmission mode to use at most locations.

Although overall SM was superior to other transmission schemes in terms of average rate on most of the paths we considered, there are cases where switching between MIMO transmission modes can bring additional gains rather than using

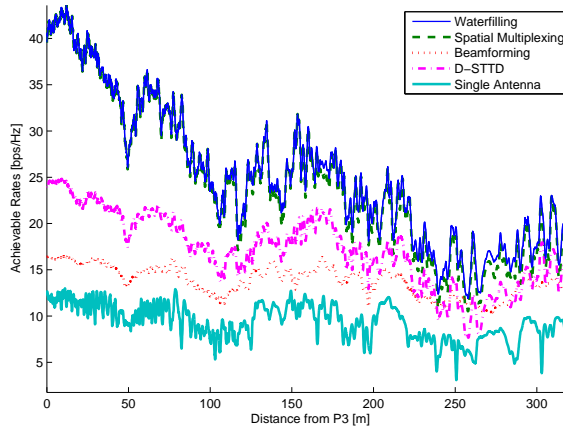


Figure 6.8: Achievable rate on the Lexington Avenue path, P3-P4, in Fig. 6.1 versus the distance from P3. Each data rate is averaged over a 1-m window. SM is seen to be the best transmission mode to use at most locations.

a fixed transmission mode. In the next section we present algorithms for switching between MIMO transmission modes.

6.3 Adapting MIMO Transmission Mode Along Paths in Urban Environments

6.3.1 Motivation

We propose some practical alternatives to waterfilling power allocation. In each scheme, the transmitter switches among diversity and spatial multiplexing modes so as to achieve good data rates as the mobile moves. The optimal switching algorithm in Section 6.3.3 gives the closest rates to the channel capacity by switching optimally between these transmission modes. The delayed feedback (DF) and probabilistic switching (PS) are more practical algorithms which do not require instantaneous channel feedback. DF chooses the next transmission state based on the average performance in the previous states. Instead, PS predicts the next transmission state from the transition probabilities and the previous state. We

refer to each of the channel matrices as a channel state.

6.3.2 Related Work

Performance gains through adapting the MIMO transmission mode has been also shown previously in [40] and [41] using stochastic channel models. Gains for other MIMO-link adaptation schemes for MIMO has been shown in [42] and [43]. In [41], the authors demonstrate theoretical capacity gains by adapting the MIMO transmission mode and propose a switching algorithm based on long term channel statistics. In [40] a switching criterion between spatial diversity and spatial multiplexing is presented that reduces the bit error rate (BER). However, the performance gains for this algorithm were shown for i.i.d path gains; this corresponds to a spatially white MIMO model, which occurs only in rich scattering environments.

6.3.3 Optimal Switching (OS)

Here, we assume we switch at each channel state to the best MIMO transmission mode, which gives the highest instantaneous rate. Such a scheme achieves the closest rates to channel capacity. We call this algorithm optimal switching. It is not very practical since it requires instantaneous channel feedback and switching at every channel state.

6.3.4 Delayed Feedback (DF)

The channel matrices tend to be spatially correlated for consecutive channel states. Therefore, the best transmission mode for a given state can be predicted from the performance of the MIMO transmission modes in the previous states instead of requiring instantaneous channel feedback.

We consider the following scenario. The transmitter has no knowledge of the

current channel state. The receiver has full or partial knowledge of the channel by decoding the pilot symbols. The receiver computes the uncoded QAM throughput for the available MIMO transmission mode from the estimated channel matrix for a given maximum modulation order [44]. The receiver feeds back the throughputs with a delay of L channel states to the transmitter. Instead, the receiver might choose to feed back to the transmitter the channel matrix \mathbf{H} and let the transmitter compute the throughputs. For each transmission mode i , the transmitter computes the average throughput $R_{avr,i}$ if that mode has been used in the previous K channel states:

$$R_{avr,i} = \frac{1}{K} \sum_{k=1}^K \delta^{k-1} R_{i,k} \quad 0 \leq \delta \leq 1 \quad (6.1)$$

By varying δ , the transmitter gives more and less weight to the data rates at the most recent channel states. For the next M channel states the transmitter switches to transmission mode i which maximizes $R_{avr,i}$ and gives at least $a\%$ average throughput increase in compare to $R_{avr,j}$ where j is the most recent used MIMO transmission mode. Switching decisions are done every M channel states as the mobile travels.

6.3.5 Probabilistic switching (PS)

Probabilistic switching algorithm requires that the receiver feeds back to the transmitter the MIMO transmission mode i which would have given the best rate at a channel state k . Let m_k be the transmission state, denoting the best performing MIMO transmission mode at the channel state k . If m_k has enough information for determining m_{k+1} without looking to the previous states, it is known as a Markov state. Let $P[m_{k+1} = i | m_k = j]$ be transition probability for switching from the transmission mode to j to i in the next channel state. The transmitter learns the transition probabilities as it moves in an environment, and updates them with every new feedback from the receiver. Formulating this as

a Markov Decision Process, at every decision state the transmitter chooses the transmission mode i which has the maximum transition probability from the state j .

6.3.6 Performance Metrics

We define following metrics:

Throughput Gains: The best fixed transmission mode is the mode which gives highest average throughput if used on all locations on a path without switching to any other mode. Let $R_{p,B}$ be the average throughput for the path p using the best fixed transmission scheme, and $R_{p,S}$ the average throughput employing the switching algorithm S . The metric $\eta_b = R_{p,S}/R_{p,B}$ gives the throughput gain in comparison to the best fixed MIMO scheme. Let $R_{p,W}$ be the average throughput for the path p using the fixed transmission scheme which gives the lowest average throughput. The metric $\eta_w = R_{p,S}/R_{p,W}$ gives the throughput gain in comparison to the fixed MIMO scheme which gives lowest average throughput.

Switching Ratio: It is desired to obtain rate increase by minimal switching since at each switching the MIMO system configuration needs to be changed. Assume the switching algorithm S requires N switches to achieve the average throughput $R_{p,S}$ on a path of L channel states. The metric $\eta_S = N/L$ is chosen as the switching ratio.

6.3.7 Results

We simulate the 4x4 MIMO channel gain matrix along the 148-m path between P5 and P7 along East 103rd Street in Fig. 6.1 using the simulation methodology and parameters as described in Section 6.2.2. We compute the throughput for a fixed modulation order of 64 QAM for BF and SM. We found that at 34.6% of locations SM was the best mode to use; at 65.4% of locations BF was superior to

spatial multiplexing. Let \mathcal{B} be the set of points on this path where BF outperforms SM, and let \mathcal{S} be the set of points where SM is superior. Average throughput at the locations in set \mathcal{B} is 3.2 bps/Hz if BF is used and 2.2 bps/Hz if SM is used. In the set \mathcal{B} , BF brings additional 45% average throughput gain in compare the SM. Average throughput at the locations in set \mathcal{S} is 6 bps/Hz if BF is used; and 8.9 bps/Hz if SM is used. In the set \mathcal{S} SM brings additional 48% average throughput gain in compare the BF. The average throughput at locations in set \mathcal{B} are much lower than the average throughput in the set \mathcal{S} .

The switching algorithms give average throughput close to the best fixed transmission mode in each set. In the set \mathcal{B} , the average throughput for OS, DF, PS is 3.2 bps/Hz, 3.18 bps/Hz, 3.17 bps/Hz, respectively. In the set \mathcal{S} , the average throughput for OS, DF, PS is 8.9 bps/Hz, 8.87 bps/Hz, 8.82 bps/Hz, respectively. The switching ratio η_S is 0.07 for OS; 0.004 for DF; and 0.06 for PS. DF requires least switching and gives average throughput close to OS in each set.

Since the average throughput in set \mathcal{B} is much lower than the average throughput \mathcal{S} , using SM at location in set \mathcal{B} would not decrease the average throughput over the entire path much. However, 45% average throughput gain by using BF in set \mathcal{B} could improve the performance at 65.4% of locations on this path.

6.4 MIMO Base Station Deployment in Urban Cells

6.4.1 Motivation

To provide good wireless coverage over an urban area using microcells, multiple bases are generally required. The dual objectives in such cases are (1) to minimize the number of bases; and (2) to determine an optimal frequency reuse plan. In the first objective, we seek to minimize both infrastructure costs and the number of handoffs in moving terminals. In the second objective, we seek to maximize overall throughput as affected by co-channel interference (CCI). Ultimately, the choice

of reuse plan is a tradeoff between the effect of CCI on link spectral efficiency (in bps/Hz) and the system-wide effect of subdividing the available spectrum among multiple channels.

Using our ray-tracing tool, we proceed in two steps: First, we use a binary integer optimization program to minimize the number of base stations such that the received SNR at every receiver location is above a specified threshold. Second, for each of the frequency reuse factors $r=1, 2, 3, 4$, we determine the reuse plan for which CCI has the least impact on overall throughput in the coverage area. The key result is a set of CDFs of total system throughput.

6.4.2 Base Deployment for a Minimum-SNR Requirement

We begin by assigning L densely-placed locations in an urban environment as candidates for base station deployment; and M densely-placed receiver locations. We want to choose those base station locations among the L candidates, such that SNR exceeds a given threshold at each of the M receiver locations. Knowing the noise power at each location, we can determine the received power required to reach the SNR requirement. We determine, for each of the M receiver locations, the locally-averaged received power from each base station, and we compare it to the required power.

Let $\mathbf{A} \in \mathbb{R}^{M \times L}$ be the matrix of locally-averaged received powers, where the i - j 'th element of \mathbf{A} gives the received power at the i^{th} receiver location from the base station j ; and let p_i be the minimum required received power at location i to reach the minimum SNR threshold. We map \mathbf{A} into the binary matrix \mathbf{B} setting the i - j 'th element of \mathbf{B} to 1 if the corresponding element in \mathbf{A} is greater than p_i ; otherwise we set it to 0. Let \mathbf{c} be a vector, with j^{th} element c_j equal to 1 if the candidate base station location j is selected, and 0 otherwise.

We formulate the binary integer problem as follows:

$$\min_{c_j \geq 0} \mathbf{c}^T \mathbf{1} \quad (6.2a)$$

$$\text{s.t. } \mathbf{B}\mathbf{c} \geq \mathbf{1}. \quad (6.2b)$$

$$c_j \in \{0, 1\} \quad (6.2c)$$

The solution for \mathbf{c} (specifically, the sum of its elements) gives the minimum number of base stations. Moreover, the locations within this column vector of the non-zero elements identify the base locations on the streets. Although the number of non-zero elements given by the solution is unique, there might be *multiple* feasible solutions, i.e., multiple sets of base locations with the same (minimum) number of bases. We choose an arbitrary one of these solutions. Further work could include searching over the feasible solutions to find the one that yields the best SINR or achievable rate distributions.

6.4.3 Frequency Reuse

For a given frequency reuse factor r , there are $R(r, K) = r^K - (r - 1)^K$ frequency reuse plans for assigning one of the r specific frequencies to each of the K base stations while also utilizing all r frequencies. For each of the $R(r, K)$ frequency reuse plans, we determine the CDF of SINR over all receiver locations. Among the $R(r, K)$ plans, we choose that one which gives the highest SINR at a chosen percentile. We repeat this for every frequency reuse factor and determine the best frequency reuse plan for each.

We determine the MIMO channel gain matrix \mathbf{H}_{ik} between each base location k and receiver locations i using the environment simulator. For a given frequency reuse plan, each receiver i chooses the frequency to operate at, and the base station to connect to, based on achieving the highest data rate.

For a $N \times N$ MIMO system the received signal \mathbf{y}_i at the receiver location i is

given by:

$$\mathbf{y}_i = \mathbf{H}_{id}\mathbf{x}_{id} + \sum_{k=1, k \neq d}^K \mathbf{H}_{ik}\mathbf{x}_{ik} + \mathbf{n}_i \quad (6.3)$$

where \mathbf{x}_{ik} is the signal intended from the base k to receiver i . We assume that each base allocates the power P equally among the transmit antennae and $E\{\mathbf{x}_{ik}\mathbf{x}_{ik}^H\} = \frac{P}{N}\mathbf{I}_N$. The noise covariance matrix is $E\{\mathbf{n}_i\mathbf{n}_i^H\} = \sigma_N^2\mathbf{I}_N$. Considering the interference from the other bases also as noise, the covariance matrix \mathbf{V} is:

$$\mathbf{V}_i = \sum_{k=1, k \neq d}^K \frac{P}{N}\mathbf{H}_{ik}\mathbf{H}_{ik}^H + \sigma_N^2\mathbf{I}_N \quad (6.4)$$

The maximum achievable rate at location i is:

$$\mathbf{R}_i = \log \left| \mathbf{I}_N + \frac{P}{N}\mathbf{H}_{id}^H\mathbf{V}_i^{-1}\mathbf{H}_{id} \right| \quad (6.5)$$

For each of the r selected frequency reuse factors, we then determine the CDF of the maximum achievable rate for spatial multiplexing over all receiver locations.

6.4.4 Results

We consider an urban neighborhood in Manhattan, as shown in Fig. 6.9, with an area of 0.5 km². We choose $L=177$ candidate base locations 40-m apart from each other and $M=856$ receivers located 13.5-m apart from each other along the streets. Note that, on some streets in Fig. 6.9 there are multiple lines of receivers. This reflects the fact that user densities might be generally higher on some streets. The base antennas are at 10-m heights; and the receiver antennas are at 2-m heights. We include the effects of diffraction and assume vertical dipole antenna elements. We determine, using the ray-tracing tool, the locally-averaged received power for each receiver-base pair. Solving (6.2), we find five base locations, such that each receiver location gets a minimum SNR of 20 dB. The selected base stations are marked with squares in Fig.6.9. We compared CDFs of SINR using the best frequency assignment strategy at each frequency reuse factor, r . There

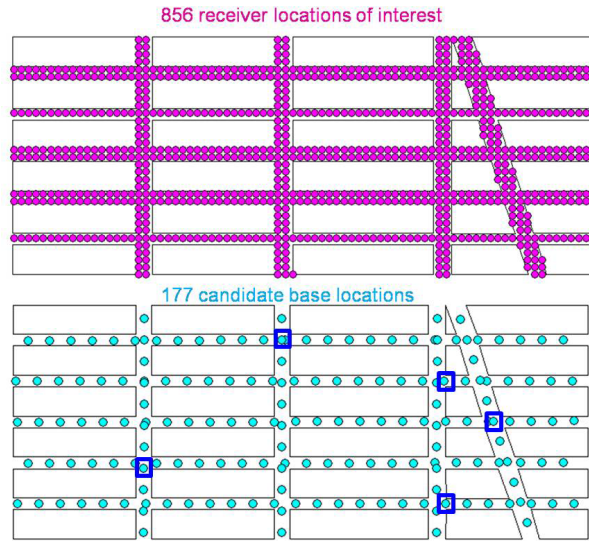


Figure 6.9: $M=856$ receiver locations and $L=177$ candidate base locations. We want to choose the minimum number of base stations such that the SNR at each receiver location is above an SNR-threshold (chosen here to be 20 dB).

is not much difference between r -values 3 and 4 in terms of median SINR, but increasing r from 1 to 2 improves the median SINR by 7 dB; and moving r from 2 to 3 improves the median SINR by an additional 2 dB. These benefits of higher r are offset by the fact that higher r means more subdivision of the available spectrum among the microcells.

We take this into account in our computations of achievable rate, in bps/Hz. In these computations, we assume that each base uses a spatial multiplexing transmission scheme with equal power on each antenna. For each of the selected frequency reuse plans, as described above, we then determine CDF's of achievable rate. Figure 6.10 shows the results for $r=1$, 4 and 4x4 MIMO. We see that $r=1$ yields a median rate that is 4.7 bps/Hz higher than for $r=2$; 7.6 bps/Hz higher than for $r=3$; and 9.3 bps/Hz higher than for $r=4$. We repeated this experiment for 3x3 MIMO, 2x2 MIMO, and single-antenna links. The frequency reuse factor 1 outperformed the others for every configuration we considered.

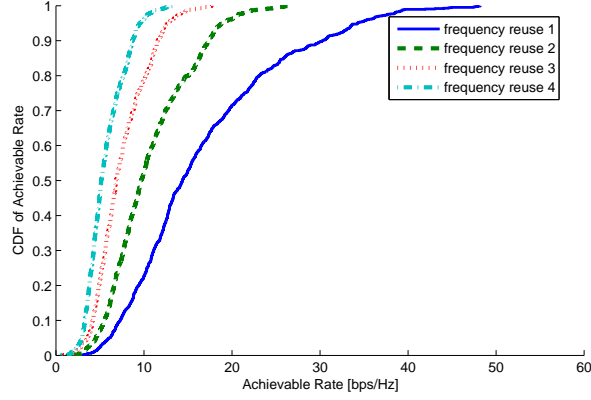


Figure 6.10: CDFs of achievable rate for system with 4x4 MIMO links for $r=1, 2, 3, 4$ (Small Area)

We repeated the experiment for a larger urban neighborhood in Manhattan with an area of 2.4 km^2 . This area is nearly five-fold larger than the neighborhood in Fig. 6.9. We used the same experiment parameters as for the 0.5 km^2 neighborhood. We chose 16 dB-minimum SNR threshold and solving (6.2) we determined 12 base station locations to cover the neighborhood fully. For the large neighborhood, this choice of minimum SNR threshold led to the highest data rates: Setting a larger minimum SNR threshold we got better SNRs, but more bases were required which reduced the SIR values. Lower minimum SNR threshold required fewer required bases and resulted in better SIR values but SNRs were poorer. Fig.6.11 shows the achievable rates for $r=1$ in the large neighborhood for various array sizes. The median rate for 4x4 MIMO is 10.41 bps/Hz. The median rate for the small neighborhood was 14.46 bps/Hz for 4x4 MIMO. For each neighborhood we computed the metric which is the sum of the average achievable rates for all the bases for 5-MHz bandwidth, divided by the area of the neighborhood. This metric is indicative of the downlink user rate. Table 6.1 shows this metric for the base station transmit power levels 10 dBm, 20 dBm and 30 dBm. The metrics for the small neighborhood at least twice larger than the

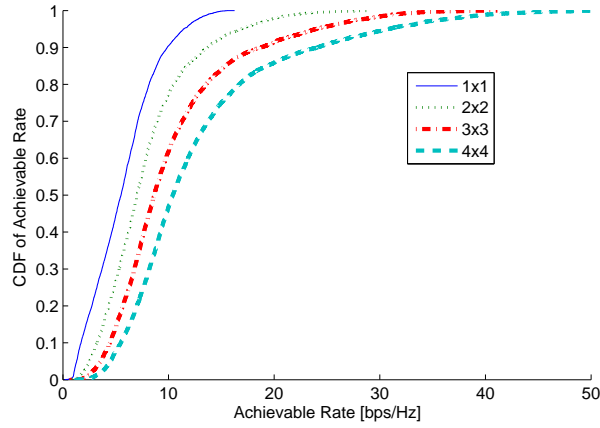


Figure 6.11: CDFs of achievable rate for various array sizes and $r=1$ (Large Area).

Table 6.1: Average Downlink Achievable Rate, in Gb/s per km^2

		Array Size			
		1x1	2x2	3x3	4x4
Small Area	10 dBm	0.33	0.51	0.69	0.89
	20 dBm	0.38	0.64	0.89	1.15
	30 dBm	0.4	0.72	1.03	1.35
Large Area	10 dBm	0.14	0.19	0.25	0.32
	20 dBm	0.17	0.25	0.34	0.44
	30 dBm	0.18	0.30	0.42	0.54

metrics for the large neighborhood.

6.5 Conclusions

We have produced a comprehensive set of results for data rate in several urban microcellular environments. Our general method can be used to research a wide range of questions and the impact of a wide array of parameters, conditions and radio techniques. We have compared location-specific MIMO performance, for varying sizes, orientations, and polarizations of the antenna arrays and for different MIMO transmission modes. We have also proposed algorithms for switching

between MIMO transmission modes along a trajectory. Finally, we have investigated the case of multiple bases, to cover a full urban neighborhood.

A major finding of our study is that a frequency reuse factor of 1 yields the best spectral efficiency in an urban microcellular environment. We conclude that CCI has less impact on the achievable rate than dividing down the available bandwidth to reduce it.

Chapter 7

Conclusions and Future Work

We have focused here on environment simulators based on ray-tracing. In particular, we have demonstrated and evaluated the use of ray tracing for both characterizing wireless channels and analyzing algorithms for various applications.

First, via comparisons with physical measurements, we demonstrated the statistical accuracy of ray-tracing predictions of channel behavior. The comparisons were made for three parameters that largely characterize a radio path's behavior: Path loss; Ricean K-factor; and RMS delay spread. The comparisons for various paths we considered showed that, the parameters predicted using the ray tracing tool agree well with measurements. This suggests that a well-designed ray-tracing program such as WiSE can be used with confidence for studying systems in indoor wireless environments. We identified two conditions that can compromise prediction accuracy of critical path properties: (1) Paths where diffraction is the primary propagation mechanism; and (2) environments for which the material properties of the walls, floor and ceiling are not well-specified. The first condition is relatively rare in indoor environments; the second condition can be avoided by using a small number of preliminary measurements, augmented by comparisons with predictions and corresponding adjustments of the assumed material properties.

Further work in this area should include, primarily, its extension to other paths and to other indoor environments. In addition, a limited amount of system studies would help to test the conjecture that the parameters studied here (path

gain, K-factor and RMS delay spread) comprise a sufficient set for capturing the properties of a channel response.

Second, we have shown by measuring the variation of the channel response that the time variations of the channel response in an indoor environment are not negligible in common scenarios such as people sitting around a table or working in an office. Therefore, the assumption of most environment-specific models that the channel response is non-varying over time if both ends of the path are fixed might be not be true in many common scenarios. We stochastically modeled the time variation of the channel response about the mean using members of the ARIMA family of processes and showed that this can lead to accurate representations. Our key finding is that ARIMA processes are capable of describing the time variation of the impulse response rays in these environments. We obtained excellent agreement using such processes for each of the categories identified and measured. Thus, one can choose to model the static indoor channel response through environment simulators and the fluctuation about it through ARIMA processes.

Note that we have not proposed specific time-variation models, but have showed via numerous measurements what kinds of processes can be used in such modeling. Extremely comprehensive measurement program spanning many environments, paths, motion scenarios and bandwidths would lead to highly useful models. Future work should include extending this work to other environments and paths.

We exploited ray-tracing for various applications in wireless systems design:

For the first application of ray-tracing, we looked to the localization of emitters in indoor environments. We presented an algorithm called Emitter Localization and Visualization (ELVIS) for localizing emitters by back-propagating the received signals via back-ray tracing. We determined that backward ray tracing can be effective even if the measured quantities such as received power, angle of arrival, time of arrival are degraded due to the fading, noise or due to the other

imperfections. The localization accuracy can be further improved by deploying multiple receivers. While the backward ray tracing technique in ELVIS produces highly accurate results using ideally accurate measurements, finite angular resolution can be a primary source of degradation. If the angular resolution is high, ELVIS provides reliable localization in 3D even with a single receiver. At lower angular resolution, multiple receivers are necessary to localize with good accuracy. We found that fading and noise are not major causes of degradation in most cases of interest.

In this work, we have defined multiple metrics based on the measured quantities and tested the localization accuracy at multiple locations in Crawford Hill building of Bell Labs, under the assumption that the blueprint of the building is perfectly known. Further work could include (1) investigation of other metrics, to improve the performance; (2) investigation of the performance in other buildings; (3) adding other error sources, such as uncertainties in the blueprint and wall properties; and (4) verification of this technique through measurements.

For the second application of ray-tracing, we presented a statistical path loss model derived from data simulated with a ray tracing tool. We collected simulated data in four large office buildings. The characterization we used is a nonlinear curve fitting of the decibel path loss to the log-distance, with a Gaussian random variation about that curve due to shadow fading. The transmission loss through the walls makes the usual linear models inappropriate for indoor scenarios. We modeled the transmission loss through the walls with an additional exponential term whose parameters show significant variations from building to building.

As future work, one could identify applications where such a modeling approach is valuable. With the methodology discussed here, a system planner can infer overall channel characteristics in a specific building. This path loss model can be used to test the performance of wireless systems and algorithms in indoor

environments. Instead of testing an algorithm in multiple buildings by doing extensive measurements or simulations, the performance can be evaluated by varying the parameters of the path loss model. Determining ranges of the parameters which correspond to realistic buildings is another topic worthy of further study.

For our last application, we looked at the performance of MIMO systems in urban microcellular environments, where we determined the location-specific channel gains by ray-tracing along various paths in Boston and Manhattan. Our primary metric was the cumulative distribution function (CDF) of achievable data rate along a particular trajectory of the mobile station. Specifically, we derived achievable downlink data rates for various conditions: Array size, array orientation, polarization, city, street, MIMO mode, and others. Our general method can be used to research a wide range of questions and the impact of a wide array of parameters, conditions and radio techniques. Also, we compared, for both line-of-sight and non-line-of-sight paths, the CDFs derived using the ray-tracing emulator with those predicted using a familiar stochastic model, i.e., i.i.d. Rayleigh fading gain matrices. We found that on NLOS paths, the CDFs have much better agreement, due to the greater amount of scatter and multipath mixing for NLOS paths. The Rayleigh assumption is wildly optimistic on LOS paths, clearly unreliable for predicting data rate results.

We also presented algorithms for adapting the MIMO transmission mode to varying channel conditions as a mobile moves along a given trajectory. We showed that by switching between diversity and spatial multiplexing modes, data rates close to channel capacity could be achieved.

Finally, we considered the case of multiple bases to cover a full urban neighborhood and investigated frequency reuse, co-channel interference and achievable rates. We presented a technique for minimizing the number of bases needed-under a specified coverage criterion-and for determining their optimal locations. We computed the neighborhood-wide CDFs of the downlink achievable rate for

different array sizes (1x1, 2x2, 3x3, 4x4) and for different frequency reuse factors $r = 1, 2, 3, 4$. We showed that $r = 1$ gives the best results for data rate, despite the higher co-channel interference, in an urban microcellular environment.

Appendix A

A.1 Models for Time Series Data

A.1.1 The Autoregressive (All-Poles) Processes, AR

The AR model pertains to an all-pole transfer function. A wide sense stationary AR process of order p is generated by passing a white noise sequence through an all-pole filter with a transfer function

$$H(z) = \frac{1}{1 + \sum_{k=1}^p a_p(k)z^{-k}}, \quad (\text{A-1})$$

where $a_p(k)$ is the k^{th} AR coefficient of the p^{th} -order filter.

The Yule Walker equations [15] provide a relationship between the filter coefficients and the autocorrelation sequence. The AR coefficients are determined by solving these equations.

A.1.2 The Moving Average (All-Zeroes) Processes, MA

The MA process refers to an all-zero transfer function. This process is generated by passing a white noise sequence through a finite impulse response (FIR) filter having a transfer function

$$H(z) = 1 + \sum_{k=1}^q b_q(k)z^{-k}. \quad (\text{A-2})$$

The Yule Walker equations for MA process are nonlinear in the model coefficients, b_q . To avoid solving non-linear equations, the coefficients can be determined from the coefficients of a higher-order all-pole filter[15].

A.1.3 The Autoregressive Moving Average Processes, ARMA

The ARMA process refers to the general case of a transfer function with both poles and zeros. A wide sense stationary ARMA (p,q) autoregressive process can be generated by passing a white noise sequence through a filter having p poles and q zeros:

$$H(z) = \frac{1 + \sum_{k=1}^q b_q(k)z^{-k}}{1 + \sum_{k=1}^p a_p(k)z^{-k}} \quad (\text{A-3})$$

An AR process is a special case of ARMA with $q = 0$; and an MA process is a special case of ARMA with $p = 0$. The filter coefficients a_q and b_q can be estimated solving Modified Yule Walker Equations (MYWE) [15].

A.1.4 ARIMA

A desired property in applying a time series model is statistical stationarity. Usually stationary time series can be described by their fixed mean, fixed variance and autocorrelation function. Many empirical series do not have a fixed mean even though they exhibit homogeneity apart from local level or trend. To make these time series stationary, the difference operator ∇ is applied d times until the data become stationary. The difference operator is defined as $\nabla x(n) = x(n) - x(n-1)$. Assume that, for a series of the d^{th} order difference, a stationary ARMA (p,q) model is obtained. The model for the nonstationary series can then be found by integrating this ARMA (p,q) process d times. Such processes are called Autoregressive Integrated Moving Average (ARIMA) (p,d,q) . It is easy to see that ARIMA is the most general class, with ARMA being the subset of ARIMA for which $d = 0$.

The entire family of models called ARIMA was proposed by Box and Jenkins [19] and is applicable to a wide variety of situations. The Box-Jenkins technique is a methodology for constructing an ARIMA process to characterize a given time series. It involves a three-step procedure, consisting of identification, model

estimation and diagnostics. Identification techniques are used to find out what particular kind of process is appropriate. They make use of the autocorrelation and partial autocorrelation functions. In the model estimation step, the parameters for each process are estimated. To find out if the fitted process adequately represent the data, diagnostic checks are done. If fit is not good, the steps are repeated again.

References

- [1] Mudhafar Hassan-Ali and Kaveh Pahlavan. A new statistical model for site-specific indoor radio propagation prediction based on geometric optics and geometric probability. *IEEE Trans. Wireless Commun.*, 1:112–124, 2002.
- [2] Gus German, Quentin Spencer, Lee Swindlehurst, and Reinaldo Valenzuela. Wireless indoor channel modeling: statistical agreement of ray tracing simulations and channel sounding measurements. In *in Proc. IEEE International Conference on Acoustics, Speech, and Signal Processing*, pages 2501–2504, 2001.
- [3] M. Hassan-Ali and K. Pahlavan. Site-specific wideband and narrowband modeling of indoor radio channel using ray-tracing. *Personal, Indoor and Mobile Radio Communications, 1998. The Ninth IEEE International Symposium on*, 1:65–68 vol.1, Sep 1998.
- [4] S.J. Fortune, D.M. Gay, B.W. Kernighan, O. Landronand, R.A. Valenzuela, and M.H. Wright. WISE design of indoor wireless systems: practical computation and optimization. *IEEE Computational Science and Engineering*, 2(1):58–68, 1995.
- [5] V. Erceg, S.J. Fortune, J. Ling, Jr. Rustako, A.J., and R.A. Valenzuela. Comparisons of a computer-based propagation prediction tool with experimental data collected in urban microcellular environments. *Selected Areas in Communications, IEEE Journal on*, 15(4), may. 1997.
- [6] Seong-Cheol Kim, Jr. Guarino, B.J., III Willis, T.M., V. Erceg, S.J. Fortune, R.A. Valenzuela, L.W. Thomas, J. Ling, and J.D. Moore. Radio propagation measurements and prediction using three-dimensional ray tracing in urban environments at 908 mhz and 1.9 ghz. *Vehicular Technology, IEEE Transactions on*, 48(3):931–946, may. 1999.
- [7] R.A. Valenzuela, D. Chizhik, and J. Ling. Measured and predicted correlation between local average power and small scale fading in indoor wireless communication channels. *Vehicular Technology Conference, 1998. VTC 98. 48th IEEE*, 3:2104–2108 vol.3, May 1998.
- [8] J. Lei, R. Yates, L. Greenstein, and H. Liu. Mapping link SNRs of wireless mesh networks onto an indoor testbed. *Conf. Rec. of TridentCom*, March 2006.

- [9] M. Ott, I. Seskar, R. Siracusa, and M. Singh. ORBIT Testbed Software Architecture: Supporting experiments as a service. *Proceedings of IEEE Tridentcom*, Feb 2005.
- [10] V. Erceg, S.J. Fortune, J. Ling, Jr. Rustako, A.J., and R.A. Valenzuela. Comparisons of a computer-based propagation prediction tool with experimental data collected in urban microcellular environments. *Selected Areas in Communications, IEEE Journal on*, 15(4):677–684, May 1997.
- [11] L. Greenstein, D. Michelson, and V. Erceg. Moment method estimation of the Ricean K-factor. *IEEE Communication Letters*, 3:175–176, June 1999.
- [12] C. Tepedelenlioglu, A. Abdi, and G. Giannakis. The Ricean K Factor: Estimation and Performance Analysis. *IEEE Trans. Commun.*, 2:799–809, July 2003.
- [13] K. Talukdar and W. Lawing. Estimation of the parameters of the Rice distribution. *J. Acoust. Soc. Am.*, 89(3):1193–1197, March 1991.
- [14] A. Saleh and R. Valenzuela. A statistical model for indoor multipath propagation. *IEEE J. Sel. Areas Commun.*, 5(2):128–137, Feb 1987.
- [15] M. H. Hayes. *Statistical Digital Signal Processing and Modeling*. John Wiley Sons, NY, USA, 1996.
- [16] S.J. Howard and K. Pahlavan. Autoregressive modeling of wide-band indoor radio propagation. *Communications, IEEE Transactions on*, 40(9):1540–1552, October 1992.
- [17] S. Ghassemzadeh, Jana R., C. Rice, W. Turin, and V. Tarokh. Measurement and modeling of an ultra-wide bandwidth indoor channel. *Communications, IEEE Transactions on*, 52(10):1786–1796, October 2004.
- [18] Z. Irahhauteh, H. Nikookar, and G.J.M. An overview of ultra wide band indoor channel measurements and modeling. *Microwave and Wireless Components Letters, IEEE*, 14(10):386–388, August 2004.
- [19] G. E. P Box and G. M. Jenkins. *Time Series Analysis Forecasting and Control*. Holden-Day Inc., San Francisco CA, USA, 1976.
- [20] H Akaike. A new look at the statistical model identification. *Automatic Control, IEEE Transactions on*, AC-19:716–723, 1974.
- [21] V. Otsason, A. Varshavsky, A. LaMarca, and E. Lara. Accurate GSM indoor localization. *UbiComp*, pages 141–158, 2005.
- [22] S. Gezici, Z. Tian, G. Giannakis, H. Kobayashi, A. Molish, V. Poor, and Z. Sahinoglu. Localization via Ultra-Wideband Radios. *IEEE Signal Processing Magazine*, 22(4):70–84, July 2005.

- [23] P. Bahl and VN Padmanabhan. Radar: An in-building RF-based user location and tracking system. *IEEE Infocom*, pages 775–784, 2000.
- [24] D. Kaspar K. Sayrafian-Pour. Indoor positioning using spatial power spectrum. *PIMRC*, 2005.
- [25] A. Madd, K. Bekris, A. Rudys, D. Wallach, and L. Kavraki. On the feasibility of using wireless ethernet for indoor localization. *Robotics and Automation, IEEE Transactions on*, 20(3):555–559, June 2004.
- [26] Aliye Özge Kaya, Larry J. Greenstein, Dmitry Chizhik, Reinaldo Valenzuela, and Nader Moayeri. Emitter localization and visualization (ELVIS): A Backward Ray Tracing Algorithm for Locating Emitters. in *Proceedings of the Conference on Information Sciences and Systems (CISS)*, pages 376 – 381, March 2007.
- [27] Vinko Erceg, Larry J. Greenstein, Sony Y. Tj, Seth R. Parkoff, Ajay Gupta, Boris Kulic, Arthur A. Julius, and Renee Bianchi. An empirically based path loss model for wireless channels in suburban environments. *IEEE Journal on Selected Areas in Communications*, 17:1205–1211, 1999.
- [28] P. Almers, E. Bonek, A. Burr, N. Czink, M. Debbah, V. Degli-Esposti, H. Hofstetter, P. Kyösti, D. Laurenson, G. Matz, A. F. Molisch, C. Oestges, and H. Özcelik. Survey of channel and radio propagation models for wireless MIMO systems. *EURASIP J. Wirel. Commun. Netw.*, 2007(1):56–56, 2007.
- [29] A. F. Molisch, A. Kuchar, J. Laurila, K. Hugl, and R. Schmalenberger. Geometry-based directional model for mobile radio channels - principles and implementation. *European Transactions on Communications*, 14(4):351–360, 2003.
- [30] C. Oestges, V. Erceg, and A.J. Paulraj. A physical scattering model for MIMO macrocellular broadband wireless channels. *Selected Areas in Communications, IEEE Journal on*, 21(5):721–729, June 2003.
- [31] A. Saleh and R. Valenzuela. A statistical model for indoor multipath propagation. *Selected Areas in Communications, IEEE Journal on*, 5(2):128–137, Feb 1987.
- [32] F.R. Farrokhi, G.J. Foschini, A. Lozano, and R.A. Valenzuela. Link-optimal space-time processing with multiple transmit and receive antennas. *Communications Letters, IEEE*, 5(3):85–87, Mar 2001.
- [33] Da-Shan Shiu, G.J. Foschini, M.J. Gans, and J.M. Kahn. Fading correlation and its effect on the capacity of multielement antenna systems. *Communications, IEEE Transactions on*, 48(3):502–513, Mar 2000.

- [34] J.P. Kermoal, L. Schumacher, K.I. Pedersen, P.E. Mogensen, and F. Frederiksen. A stochastic MIMO radio channel model with experimental validation. *Selected Areas in Communications, IEEE Journal on*, 20(6):1211–1226, Aug 2002.
- [35] W. Weichselberger, M. Herdin, H. Ozelik, and E. Bonek. A stochastic MIMO channel model with joint correlation of both link ends. *Wireless Communications, IEEE Transactions on*, 5(1):90–100, Jan. 2006.
- [36] C.C. Martin, J.H. Winters, and N.R. Sollenberger. MIMO radio channel measurements: performance comparison of antenna configurations. volume 2, pages 1225–1229 vol.2, 2001.
- [37] N. Amitay, L.J. Greenstein, and G.J. Owens. Measurement-based estimates of bit-error-rate performance in urban LOS microcells at 900 mhz. *Vehicular Technology, IEEE Transactions on*, 41(4):414–423, Nov 1992.
- [38] E.N. Onggosanusi, A.G. Dabak, and T.A. Schmidl. High rate space-time block coded scheme: performance and improvement in correlated fading channels. In *Wireless Communications and Networking Conference, 2002. WCNC2002. 2002 IEEE*, volume 1, pages 194–199 vol.1, Mar 2002.
- [39] Andrea Goldsmith. *Wireless communications*. Cambridge University Press, NY, USA, 2005. Ch. 10.4.
- [40] R.W. Heath and A.J. Paulraj. Switching between diversity and multiplexing in MIMO systems. *Communications, IEEE Transactions on*, 53(6):962–968, June 2005.
- [41] A. Forenza, M.R. McKay, A. Pandharipande, Jr. Heath, R.W., and I.B. Collings. Adaptive MIMO transmission for exploiting the capacity of spatially correlated channels. *Vehicular Technology, IEEE Transactions on*, 56(2):619–630, March 2007.
- [42] Jr. Heath, R.W., S. Sandhu, and A. Paulraj. Antenna selection for spatial multiplexing systems with linear receivers. *Communications Letters, IEEE*, 5(4):142–144, Apr 2001.
- [43] S. Catreux, V. Erceg, D. Gesbert, and Jr. Heath, R.W. Adaptive modulation and MIMO coding for broadband wireless data networks. *Communications Magazine, IEEE*, 40(6):108–115, Jun 2002.
- [44] S. Catreux, P.F. Driessen, and L.J. Greenstein. Simulation results for an interference-limited multiple-input multiple-output cellular system. *Communications Letters, IEEE*, 4(11):334 –336, nov 2000.
- [45] Aliye Özge Kaya, Wade Trappe, and Larry J. Greenstein. Adapting MIMO Transmission Mode Along Paths in Urban Environments. in *Proceedings of*

the IEEE International Conference on Acoustics, Speech, and Signal Processing (ICASSP), pages 3462 – 3465, March 2010.

- [46] Aliye Özge Kaya, Mung Chiang, and Wade Trappe. P2P-ISP Cooperation: Risks and Mitigation. *in Proceedings of the IEEE Global Telecommunications Conference (GLOBECOM)*, Dec. 2009 (**BEST PAPER AWARD**).
- [47] Aliye Özge Kaya, Larry J. Greenstein, and Wade Trappe. Characterizing Indoor Wireless Channels via Ray Tracing Combined with Stochastic Modeling. *IEEE Transactions on Wireless Communications*, 8(8):4165 –4175, August 2009.
- [48] Aliye Özge Kaya, Larry J. Greenstein, and Wade Trappe. Characterizing Indoor Wireless Channels via Ray Tracing, and Validation via Measurements. *in Proceedings of the IEEE Global Telecommunications Conference (GLOBECOM)*, Dec. 2008.
- [49] Aliye Özge Kaya, Larry J. Greenstein, and Wade Trappe. Modeling Temporal Channel Variations in Indoor Wireless Environments. *in Proceedings of the IEEE Military Communications Conference (MILCOM)*, Nov. 2008.

Curriculum Vita

Aliye Özge Kaya

Education

- Ph.D., Electrical and Computer Engineering, Oct. 2010
Wireless Information Network Laboratory (WINLAB), Rutgers University,
New Brunswick, NJ., USA
- M.Sc., Electrical and Computer Engineering, May 2010
Wireless Information Network Laboratory (WINLAB), Rutgers University,
New Brunswick, NJ., USA
- Dipl. Ing. Univ., Electrical Engineering and Information Technology,
Nov. 2003
Munich University of Technology (TUM), Munich Germany
- B.Sc., Electrical Engineering and Information Technology, Feb. 2003
Munich University of Technology (TUM), Munich Germany

Work Experience

- WINLAB, Rutgers University, North Brunswick, NJ
Graduate Assistant, Jan. 2005 - Sept. 2010
- ECE Department, Rutgers University, Piscataway, NJ
Teaching Assistant, Instructor, Spring, Summer 2009
- InterDigital Communications Corp., CTO Office, King of Prussia, PA
Intern, Jun. 2006 - Jan. 2007
- Bell Laboratories, Alcatel-Lucent, Holmdel, NJ
Intern, Oct. 2005 - Jun. 2006
- Siemens USA-Corporate Research Center, NYC, NY- Princeton, NJ
Intern, Nov. 2003 - Dec. 2004
- Siemens Mobile Germany, Ulm, Germany
Intern, May 2003 - Nov. 2003

Publications

- Aliye Özge Kaya, Wade Trappe, and Larry J. Greenstein, “Adapting MIMO Transmission Mode Along Paths in Urban Environments,” *in Proceedings of the IEEE International Conference on Acoustics, Speech, and Signal Processing (ICASSP)*, pp. 3462-3465, March 2010.
- Aliye Özge Kaya, Mung Chiang, and Wade Trappe, ”P2P-ISP Cooperation: Risks and Mitigation,” *in Proceedings of the IEEE Global Telecommunications Conference (GLOBECOM)*, Dec. 2009 (BEST PAPER AWARD).
- Aliye Özge Kaya, Larry J. Greenstein, and Wade Trappe, “Characterizing Indoor Wireless Channels via Ray Tracing Combined with Stochastic Modeling,” *IEEE Transactions on Wireless Communications*, vol. 8, no. 8, pp. 4165-4175, August 2009.
- Aliye Özge Kaya, Larry J. Greenstein, and Wade Trappe, “Characterizing Indoor Wireless Channels via Ray Tracing, and Validation via Measurements,” *in Proceedings of the IEEE Global Telecommunications Conference (GLOBECOM)*, Dec. 2008.
- Aliye Özge Kaya, Larry J. Greenstein, and Wade Trappe, “Modeling Temporal Channel Variations in Indoor Wireless Environments,” *in Proceedings of the IEEE Military Communications Conference (MILCOM)*, Nov. 2008.
- Aliye Özge Kaya, Larry J. Greenstein, Dmitry Chizhik, Reinaldo Valenzuela, and Nader Moayeri, “Emitter localization and visualization (ELVIS): A Backward Ray Tracing Algorithm for Locating Emitters,” *in Proceedings of the Conference on Information Sciences and Systems (CISS)*, pp. 376-381, March 2007.